(L.O. Copy) Mr. R.J. Templin

L.O. NAE-225-1 FILE BM49-10R-1 PREPARED BY JGL & DWB CHECKED BY JL	NATIONAL AERONAUTICAL ESTABLISHMENT OTTAWA, CANADA LABORATORY MEMORANDUM SECTION Aerodynamics	AE-46d NO. HSAL-M-58 PAGE 1 OF 24 COPY NO. 1 DATE 24 October 1955

SECURITY CLASSIFICATION ~~SECRET~~

SUBJECT Supersonic Wind Tunnel Tests of the 1/40 scale Intake Model of the C-105 Aircraft

PREPARED BY J. G. LaBerge
D. W. Boyer

ISSUED TO Mr. J. H. Parkin
Dr. D. C. MacPhail
Mr. J. R. Templin (2)
Mr. J. Lukasiewicz (2)
Authors (2)
Aero Library (2)
Mr. J. Chamberlain, AVRO Aircraft (3)

Summary

In order to assess the supersonic performance of the C-105 intakes, pressure recovery and drag were measured on a 1/40 scale intake model over a range of mass flows and Mach numbers. Also, the stability of the flow was investigated in an attempt to determine the onset of "buzz" and schlieren photographs of the flow were taken.

Early in the test programme the velocity distribution in the intake ducts was found to be unsatisfactory. The programme, in a somewhat abbreviated form, was carried through nonetheless to determine the orders of magnitude involved and possibly to discover the cause of the poor distribution. The latter was attributed to poor dimensional accuracy of the model; in particular, the matching of the flow surfaces in the ducts downstream of the model intake was not satisfactory.

Contents

List of Illustrations

List of Illustrations (Cont'd)

List of Symbols

A	Cross-Sectional Area, $in.^2$
C_D	External drag coefficients defined by Eq. (11)
D	External drag force, lbs.
F	Force measured by drag balance, lbs.
g	Acceleration due to gravity, 32.2 $lbs/sec.^2$
γ	Ratio of specific heats, $C_p/C_v = 1.4$
L	Length of diffuser, from minimum section to constant area section, in.
m	Mass flow, slugs/sec.
M	Mach number
n	Location of area divisions and associated probes, Fig.4
p	Static pressure, psia
p_o	Total pressure, psia
q	Dynamic pressure, $\frac{\gamma}{2} p M^2$, psia
R	Gas constant
ρ	Density
S	Location of choking plugs, Fig.1
T_o	Total temperature, °R
θ	Angular location of pitot probes, positive counter clockwise looking upstream
V	Velocity, ft/sec.
x	Distance downstream of intake entry plane, in.

Subscripts

∞	Free stream conditions
A_2	Intake entry area, 0.592 $in.^2$

A_3 Intake area at measuring station 3, 0.636 in.^{2}

A_b Base area of model minus area of intake ducts at exit, 3.82 in.^{2}

A_F Maximum frontal area of model, 5.09 in.^{2}

A_5 Exit area as a function of S

A_x Cross-sectional area of diffuser at station x, in.^{2}

A_{max} Maximum cross-sectional area of diffuser at x = L, in.^{2}

Superscripts

$( )^*$ Critical conditions

1. Introduction

A 1:40 scale model of the intake of the C-105 aircraft was suitably instrumented so that the following tests could be carried out: (a) Measurement of intake pressure recovery and duct losses, (b) Dynamic pressure measurements indicating onset of "buzz", and (c) External drag. These tests were performed at nominal Mach numbers of 1.4, 1.6 and 1.8 with a constant ramp angle of 12°. The range of mass flow through the intakes was sufficiently large to encompass the regions of interest. The effects of incidence and boundary layer bleed flow were explored.

The test Reynolds number was about 1.4×10^6 based on the distance from model nose to ramp lips.

2. Test Model

This is shown schematically in Fig. 1 where also are indicated the model stations corresponding to the arbitrarily selected flow stations. A photograph of the model fully instrumented and mounted on the balance is seen in Fig. 2. Mass flow through the intakes was varied by means of choking plugs at the exits which could be adjusted to give any desired value of exit area. Both plugs were always moved together.

The value of "S" shown in the inset of Fig. 1 is a measure of the downstream axial movement of the plugs expressed in fractions of an inch.

The port plug was allowed to slide over four pitot probes which were fixed axially with respect to the duct and positioned 90° apart at varying radii. The impact faces of the probes were all located in the plane of the three static orifices in the duct wall. Furthermore, at any plug setting the probes could be rotated in unison through an angle of 360° thus allowing a complete circumferential traverse at four different radii.

The starboard plug carried no instrumentation as it was used only to adjust the mass flow to the value obtained in the port duct. However, a pressure cell sensitive to pressure oscillations was incorporated in the starboard duct in order to detect the onset of "buzz". This is shown schematically in the inset in Fig. 22(a). As the terminal posts of this cell protruded into the airstream on top of the fuselage, a plasticine fairing was put over it necessitating a similar fairing on the port side in order to preserve symmetry.

Although the model was designed to accommodate interchangeable ramps of various lip angle only the 12° ramps, representative of the actual aircraft configuration, were used in the tests. On assembling the ramps to the intakes all joints were carefully sealed with "Sealite" cement.

Mass flow through the boundary layer bleed ducts was varied in discrete steps by the introduction of two sets of brass inserts into the boundary layer bleed duct exit. Thus the mass flows achieved were those with the ducts fully open, fully closed and half open, i.e., with the exit area set at half the fully open value. A single pitot probe was located on the axis of the port bleed duct the forward face of which was positioned in the plane of the four wall static orifices. When the duct was fully closed this probe was withdrawn.

In all, there were seven static pressure orifices in both the intake and boundary layer bleed ducts which were connected to steel hyperdermic tubing running through the solid portion of the model. These tubes protruded about 1/4 inch into the airstream where connections to plastic tubing were made. In Fig. 2 the choking plugs have been interchanged to show the model more clearly.

3. Wind Tunnel

The model was tested at three Mach numbers in the 10 inch supersonic tunnel, the corresponding Reynolds number being about 1.4×10^6 based on the distance from fuselage nose to ramp lips. The nominal and actual Mach numbers as well as the percent variation in Mach number in the tunnel working section were as follows:

M - Nominal	1.4	1.6	1.8
M - Mean	1.44	1.64	1.83
%M	$\pm$1.2	$\pm$0.9	$\pm$0.7

The model was interference-free at all Mach numbers; the tunnel air was dried to a specific humidity of less than 0.0005, the stagnation pressure and temperature being approximately atmospheric. Runs of about 10 seconds duration were taken.

4. Balance and Model Mounting

As drag measurements were to be made later on in the test programme, the drag balance, although inactive, provided a convenient mount for the model whilst the initial pressure measurements were carried out and schlieren observations made.

This balance could rotate the model through an angle of attack range from 0° to nearly 10° as well as through 360° in roll.

The model was sting-mounted to this balance with the bracket holding the choking plugs, referred to above, attached to the shield of the sting. Thus the plugs were completely separated from the model-sting combination. Also by means of the shield the pressure existing on the base of the model could be measured.

5. Test Procedure

It was not found feasible to take various sets of measurements concurrently. Hence the test programme was divided as follows: Pressure measurements through the complete range of test configurations were made first. For this purpose all pressure taps on the model were connected to short small-bore plastic tubing and carried outside the airstream where connections were made to large-bore rubber tubing. These then led directly to a multiple tube mercury manometer. At each position of the choking plugs, which were moved from S = 0.5 to S = 0.9 inclusively, readings were taken at every 90° rotation of the port plug.

When the above measurements had been completed, model drag was recorded for the same range of S. For this purpose all pressure leads were removed and pressure taps on the model were blocked off. Shield pressure, however, was measured. The balance output, as given by a displacement transducer, was carried to a high speed potentiometer recorder. Similarly the shield pressure, which was measured with a pressure transducer, was carried to a second recorder. These recorders provided reading accuracies up to + 0.2%. All tests were carried out at incidences of 0° and +4°.

Following the drag measurements, tests on flow stability were made again for the same range of S. These tests were carried out using a 2.5 p.s.i. Sierra pressure cell mounted in the star board duct. The pressure oscillations were recorded by feeding the output of the Sierra bridge circuit into an oscillograph.

For a particular Mach number and plug setting the inner chamber or reference pressure was maintained at the duct static pressure determined from the preceding pressure tests. This ensured that the cell diaphragm was unloaded statically during a run and responded only to dynamic pressures.

Finally, schlieren photographs were taken for S settings of 0.5, 0.7 and 0.9 for various conditions of boundary layer bleed flows and external boundary layers over the range of test Mach numbers. These photographs were limited to a model incidence of 0° inasmuch as the model had to be rotated 90° in order to show the details of the flow at the intake entries. Illumination was provided by a spark source.

6. Data Reduction

6.1 Mass Flow Ratio

From the usual isentropic relations for a perfect gas the following expression can easily be shown to hold,

$$m = \rho A V = \sqrt{\frac{2\gamma}{(\gamma-1)gRT_0}}\; A p \left\{\left(\frac{p_0}{p}\right)^{\frac{\gamma-1}{\gamma}}\left[\left(\frac{p_0}{p}\right)^{\frac{\gamma-1}{\gamma}} - 1\right]\right\}^{\frac{1}{2}} \qquad (1)$$

Referring to Figure 3, the mass flow at station 3 will be,

$$m_3 = \sqrt{\frac{2\gamma}{(\gamma-1)gRT_0}}\; A_3 p_3 \left\{\left(\frac{p_{02}}{p_3}\right)^{\frac{\gamma-1}{\gamma}}\left[\left(\frac{p_{03}}{p_3}\right)^{\frac{\gamma-1}{\gamma}} - 1\right]\right\}^{\frac{1}{2}} \qquad (2)$$

Define

$$m_\infty = A_2 \rho_\infty V_\infty \qquad (3)$$

i.e. The mass flowing in the free-stream through an area equal to that of the flow area at station 2.

Hence,

$$m_\infty = \sqrt{\frac{2\gamma}{(\gamma-1)gRT_0}}\; A_2 p_\infty \left\{\left(\frac{p_{0\infty}}{p_\infty}\right)^{\frac{\gamma-1}{\gamma}}\left[\left(\frac{p_{0\infty}}{p_\infty}\right)^{\frac{\gamma-1}{\gamma}} - 1\right]\right\}^{\frac{1}{2}}$$

or

$$m_\infty = \sqrt{\frac{\gamma}{gRT_0}}\; A_2 p_\infty M_\infty \left[1 + \frac{\gamma-1}{2} M_\infty^2\right]^{-\frac{(\gamma+1)}{2(\gamma-1)}} \qquad (4)$$

Dividing Eq. (3) by Eq. (4) and simplifying, the mass flow ratio is,

$$\frac{m_3}{m_\infty} = K_i f(M_\infty) \frac{p_3}{p_{0\infty}} \left\{\left(\frac{p_{03}}{p_3}\right)^{\frac{\gamma-1}{\gamma}}\left[\left(\frac{p_{03}}{p_3}\right)^{\frac{\gamma-1}{\gamma}} - 1\right]\right\}^{\frac{1}{2}} \qquad (5)$$

where

$$K_i = \sqrt{\frac{2}{\gamma-1}}\; \frac{A_3}{A_2}$$

and

$$f(M_\infty) = \frac{\left(1 + \frac{\gamma-1}{2} M_\infty^2\right)^{\frac{\gamma+1}{2(\gamma-1)}}}{M_\infty}$$

The free-stream Mach number function is given in the table below for $\gamma = 1.4$,

M_∞	$f(M_\infty)$
1.44	1.958
1.64	2.212
1.83	2.523

However, as each of the four pitot probes in the instrumented duct is effectivo over areas of different magnitude tho overall mass flow ratio is found more precisely by summing tho component mass flow ratios over small area divisions such as indicated on Figure 4. Moreovor, since readings were takon at every 90° for $0° \leq \theta \leq 270°$, where θ is the angular displacement of the pitot tube assembly, the mass flow ratios through the area divisions become,

$$\left(\frac{m_3}{m_\infty}\right)_\theta = (K_n)_\theta \, f(M_\infty) \left(\frac{\bar{p}_3}{p_{0\infty}}\right) \left\{ \left(\frac{p_{03,n}}{\bar{p}_3}\right)_\theta^{\frac{\gamma-1}{\gamma}} \left[\left(\frac{p_{03,n}}{\bar{p}_3}\right)_\theta^{\frac{\gamma-1}{\gamma}} - 1 \right] \right\}^{\frac{1}{2}} \qquad (6)$$

$n = 1, 2, 3, 4$

$\theta = 0°, 90°, 180°, 270°$

where $\bar{p}_3$ is the arithmetic moan of the static pressure readings and

$$K_n = \sqrt{\frac{2}{\gamma-1}} \, \frac{A_{3,n}}{A_2}$$

The value of K_n is tabulated below for a measured intake entry area $A_2 = 0.592$ in.^{2} ✱

n	K_n
1	0.04816
2	0.08564
3	0.12900
4	0.33804

6.2 Mass Flow Weighted Pressure Recovery

The pitot pressures were mass flow-weighed to give the overall pressure rocovery according to the following expression,

$$\frac{\bar{p}_{03}}{p_{0\infty}} = \frac{\sum_{\theta=0}^{\theta=270} \sum_{n=1}^{n=4} \left(\frac{m_{3,n}}{m_\infty}\right)_\theta \left(\frac{p_{03,n}}{p_{0\infty}}\right)_\theta}{\sum_{\theta=0}^{\theta=270} \sum_{n=1}^{n=4} \left(\frac{m_{3,n}}{m_\infty}\right)_\theta} \qquad (7)$$

✱ This area was determined by measuring the area of the template used in the manufacture of tho intake entry. It corresponds to 947 in.^{2} or 6.58 ft.^{2} full scale.

6.3 Assumption of Sonic Velocity at Duct Exit

6.3.1 Mass Flow Ratio

The mass flow ratio can also be calculated by considering the intake exit to be choked. Under this condition one needs the area ratio between stations 3 and 5 (to determine the Mach number at station 3) and the static pressure at station 3. The mass flow ratio thus becomes

$$\frac{m_3}{m_\infty} = \frac{m_5}{m_\infty} = \frac{A_5 \rho_5 V_5}{A_2 \rho_\infty V_\infty} = \frac{A_5}{A_2} \frac{\rho^* V^*}{\rho_\infty V_\infty} \qquad (8)$$

Eq. (8) can easily be shown to be equivalent to

$$\frac{m_3}{m_\infty} = \frac{A_5}{A_2} \frac{p_{05}}{p_{0\infty}} \frac{1}{M_\infty} \left(\frac{2}{\gamma+1} + \frac{\gamma-1}{\gamma+1} M_\infty^2 \right)^{\frac{\gamma+1}{2(\gamma-1)}} \qquad (8a)$$

If it is assumed that the total pressure loss between stations 3 and 5 is negligible we have

$$\frac{m_3}{m_\infty} = \frac{A_5}{A_2} \frac{p_3}{p_{0\infty}} \frac{p_{03}}{p_3} h(M_\infty) \qquad (9)$$

The free-stream Mach number function, h (M_∞), for $\gamma = 1.4$ is given in the table below.

M	h (M_∞)
1.44	1.138
1.64	1.283
1.83	1.473

The area ratios A_3/A_5 and A_5/A_2 are functions of the exit plug setting, S, and are given in the table below

S	A_3/A_5	A_5/A_2
0.50	2.426	0.443
0.60	1.818	0.591
0.70	1.436	0.748
0.75	1.304	0.824
0.80	1.217	0.883
0.90	1.066	1.008

By definition, Eq. (3), we have

$$\frac{m_3}{m_\infty} = \frac{\rho_3 V_3 A_3}{\rho_\infty V_\infty A_2} = \frac{\rho_\infty V_\infty A_\infty}{\rho_\infty V_\infty A_2} = \frac{A_\infty}{A_2}$$

Therefore,

$$A_\infty = \frac{m_3}{m_\infty} A_2 \qquad (12)$$

Eq. (11) becomes,

$$D = F + 2A_3(2q_3 + p_3) - \frac{m_3}{m_\infty} A_2 (4q_\infty + p_\infty) - (A_3 + A_b) p_\infty + A_b p_b$$

So that

$$C_D = \frac{F}{q_\infty A_F} + \frac{2A_3}{A_F}\left(2\frac{\bar{q}_3}{q_\infty} + \frac{p_3}{q_\infty}\right) - \frac{\bar{m}_3}{m_\infty}\frac{A_2}{A_F}\left(4 + \frac{2}{\gamma M_\infty^2}\right) - \left(\frac{A_3 + A_b}{A_F}\right)\frac{2}{\gamma M_\infty^2} + \frac{A_b}{A_F}\frac{p_b}{q_\infty} \qquad (13)$$

where $\frac{\bar{q}_3}{q_\infty}$ is the area-weighted dynamic pressure ratio

and $\frac{\bar{m}_3}{m_\infty}$ is the sum of the component mass flow ratios as given by the denominator of Eq. (7)

The area-weighed dynamic pressure ratio was calculated from the following expression,

$$\frac{\bar{q}_3}{q_\infty} = \frac{\sum_{\substack{n=1 \\ \theta=0}}^{\substack{n=4 \\ \theta=270}} \left[A_{3,n}\left(\frac{q_{3,n}}{q_\infty}\right)\right]_\theta}{\sum_{\substack{n=1 \\ \theta=0}}^{\substack{n=4 \\ \theta=270}} (A_{3,n})_\theta} = \frac{\sum_{\substack{n=1 \\ \theta=0}}^{\substack{n=4 \\ \theta=270}} \left[A_{3,n}\left(\frac{q_{3,n}}{p_\infty}\right)\right]_\theta}{a A_3} \qquad (14)$$

where $a = \frac{q_\infty}{p_\infty}$ = function of M_∞

Now, since $\frac{p_{o3}}{p_3} = \left(1 + \frac{\gamma-1}{2} M_3^2\right)^{\frac{\gamma}{\gamma-1}}$

and $q_3 = \frac{\gamma}{2} p_3 M_3^2$

we have $q_3 = \frac{\gamma}{\gamma-1} p_3 \left[\left(\frac{p_{o3}}{p_3}\right)^{\frac{\gamma-1}{\gamma}} - 1\right]$

and $\frac{q_3}{q_\infty} = \frac{\gamma}{\gamma-1} \frac{p_3}{p_\infty}\left[\left(\frac{p_{o3}}{p_3}\right)^{\frac{\gamma-1}{\gamma}} - 1\right]$

Hence,

$$\frac{\bar{q}_{\delta_3}}{q_\infty} = \frac{3.5 \sum_{\theta=0}^{\theta=270} \sum_{n=1}^{n=4} (A_{3,n})_\theta \left(\frac{\bar{p}_3}{p_\infty}\right)\left[\left(\frac{p_{o_{3,n}}}{\bar{p}_3}\right)^{\frac{\gamma-1}{\gamma}} - 1\right]}{a A_3} \qquad (15)$$

7. Discussion of Results

7.1 Total Pressure Distribution

Figures 5 to 11 inclusive give the ratio of total to static pressures across horizontal and vertical diameters at sta. 3 for a range of mass flows* and Mach numbers as well as for various model configurations. All these figures have one feature in common, namely, very poor pressure distributions, particularly at the higher mass flows.

Figure 5 presents these distributions at a free stream Mach number of 1.44 for full boundary layer bleed mass flow and with the fusolage datum set at zero incidence. It will be seen that there existed a very large drop in total pressure in the vicinity of the duct axis which became particularly serious at high mass flows. Similar flow patterns were found at Mach numbers of 1.64 and 1.83 with perhaps slight variations in the location of the largest pressure dip.

Figure 6 shows the effect of completely closing the boundary layer bleed ducts at a Mach number of 1.83 and at zero angle of incidence as indicated by the dashed line. This effect appeared to be a general increase of the pressure ratio (i.e. local Mach number) over the whole range of mass flows through the intakes without a significant change in the quality of the pressure distributions.

The influence of the external boundary layer on the total pressure distribution is shown in Figure 7 for a free stream Mach number of 1.64. The model was set for zero incidence and for full boundary layer bleed mass flow. Here a turbulent boundary layer on the fuselage was induced by means of a band of sand particles round the fuselage nose. A similar boundary layer was produced on the ramps by bonding a wire across the inclined face of the ramps at a point about three sixteenths of an inch downstream of the ramp lips.

As can be seen the type of external boundary layer had a small effect on the pressure distribution except at the highest mass flows where the turbulent boundary layer increased the magnitude of the largest depression in the distribution.

* The mass flow ratios corresponding to plug positions 1' are given in Figure 27.

The effects of incidence are indicated in Figure 8 which is plotted for a free stream Mach number of 1.64, full boundary layer bleed mass flow and induced transition on fuselage nose and on ramps. Increasing the incidence from 0° to 4° appeared to smooth out the pressure distribution at the smallest mass flows but did not seem to produce any improvement at the other end of the range; in fact in some instances the pressure dips were accentuated.

In exploring all the factors which could conceivably account for the very unsatisfactory pressure distributions which were being measured, the model was thoroughly tested for leaks by immersion in an oil bath. The intake entries were successively plugged with shaped rubber slugs while compressed air was let into the duct exits. This test revcaled serious leaks bctween intake and boundary bleed ducts on both sides of the model. Upon completely dismantling the model it was found that the solder used in sealing the joints had not penetrated a sufficient distance into the inner portions to effect a completc seal.

Consequently,all joints were coated with "Sealit" cement and the model rc-assembled. Tests subsequently performed,however, indicated that leakage was not responsible for the poor pressure distributions, as can be seen in Figure 9.

In order to impart to that portion of the boundary layer not captured by the bleed duct a smoother outward flow over the fuselage sides, the boundary layer bleed duct entry configuration was modified as shown in Figure 10. Total pressure measurements with the modified ramps, Figure 11, were essentially unchanged when compared to those measurcd with the original ramps.

It was concluded, therefore, that the nature of the pressure distributions was due to the internal configuration of the intake ducts, as determined by the design area distribution and matching of the internal flow surfaces. The relative effects of the above two factors could not be, however, determined from the tests.

The area distribution of the C-105 intake ducts, as given in Reference 1, was compared to those of models used in References 2 and 3. The configurations of the latter models were similar to that of the C-105 model and gave good pressure distributions. The comparison is shown in Figure 12 where areas and lengths are plotted non-dimensionally to the scale of the C-105 model. Except for the curvature of the C-105 distribution being opposite to that of the two other intakes. the C-105 duct area variation is in general similar to that of the NACA models (Ref. 2 and 3). The C-105 design would result in relatively larger adverse pressure gradient in the upstream portion of the duct.

The matching of the internal duct surfaces in the model was observed to be poor. The consistently large dip in the pressure distribution occurring at the high mass flows slightly below and to the left of the duct axis was probably caused by the very bad joint where two parts of the model came together to form the internal duct.

7.2 Pressure Recovery

Corresponding to the pressure distributions discussed above, the mass flow-weighted pressure recoveries calculated by means of Eq. 7 are plotted against mass flow ratio in Figures 13 to 18 inclusive.

In Figure 13 are shown the pressure recoveries for the three test Mach numbers, with full boundary layer bleed flow and at zero incidence. Peak pressure recoveries decreased from 0.944 to 0.820 as the Mach number was increased from 1.44 to 1.83, the mass flow ratios corresponding to the peak recoveries increasing from 0.65 to 0.92, the latter occurring at a Mach number of 1.64.

For comparison, the pressure recoveries computed under the assumption of sonic flow at the intake duct exit are represented by dashed lines in the same figure. The agreement is reasonably good at the low mass flow ratios. However, at the higher mass flow ratios it is doubtful that the flow reached sonic velocity at the exit. This would presumably explain the lack of agreement particularly noticeable at the lowest Mach number.

Because of the uncertainty as to the range of validity of the assumption made in Section 6.3 above, pressure recoveries were computed by the mass flow-weighted method.

The effect of mass flow through the boundary layer bleed ducts on pressure recovery is shown in Figure 14. At a Mach number of 1.83 and with the model at zero incidence, peak pressure recoveries increased from 0.735 to 0.820 as the mass flow through the bleed ducts increased from zero to the maximum value. With increasing mass flow ratios through the intakes, the improvement in pressure recovery due to maximum bleed flow increased from 5.5 to 11.2%.

Artifically inducing transition had a deleterious effect on pressure recovery as can be seen in Figure 15. Here the pressure recoveries are shown for natural and induced transitions at a Mach number of 1.64, zero incidence and full boundary layer bleed flow. The loss in recovery brought about by induced transition varied between 3 and 10% over the mass flow ratio range explored.

A change of incidence from 0° to +4° produced no change in the pressure recovery as shown in Figure 16 which is plotted for a

Mach number of 1.64 and for full boundary layer bleed flow with induced external transition. The effect of incidence on pressure recovery was therefore much smaller than it was on the total pressure distribution, Figure 8.

Similarly, leakage between intake and boundary layer bleed ducts produced no significant change in the pressure recovery as is evident in Figure 17. Here flow conditions and model configuration correspond to those of Figure 9.

Replacing the original ramp by the modified one produced a modest improvement in the pressure recovery, giving an increase of 2% in the peak values, Figure 18. This comparison was made at a Mach number of 1.64, incidence of +4°, full boundary layer bleed flow and natural transition. In both instances the model was re-sealed.

7.3 External Drag Coefficient

The external drag coefficient* at zero incidence and with full boundary layer bleed flow was calculated by means of Eq. (13) and plotted against the mass flow ratio in Figure 19. The corresponding pressure recovery characteristics are given by Figure 13.

The external drag is seen (Figure 19) to decrease with mass flow increasing and to reach, at least at Mach numbers of 1.44 and 1.64, a minimum at the point beyond which the pressure recovery abruptly decreases, see Figure 13. In view of the protuberances on the model (pressure tubes, fairings over the Sierra pressure cell, etc.) and the unknown base pressure distribution, the absolute values of the measured drag are of little interest. It is suggested, however, that the slope of the $C_D - \bar{m}_3/m_\infty$ curves is of significance. It is found that a decrease of 0.1 in the mass flow ratio causes an increase of about 0.0018 in the external drag coefficient based on the wing area.

The calculation of the external drag coefficient involves a large number of terms, as shown in section 6.4, and their variation with mass flow ratio is shown in Figure 20 for $M_\infty = 1.44$. The drag force as measured, term 1, shows a variation similar to the external drag coefficient, Figure 19. The base pressure, term 6, appears to be increasing slightly with the mass flow increasing.

7.4 Flow Stability

Oscillograph records of pressure fluctuations were measured with the Sierra cell at nominal Mach numbers of 1.4, 1.6 and 1.8 for zero and full boundary layer bleed flow and for choking plug settings from S = 0.5 to S = 0.9. The results of those tests are summarized in Table 1 and some of the oscillograph traces are reproduced in Figures 21 and 22.

* Based on the maximum cross-sectional area of the model.

All records, Table 1, exhibited an approximately constant frequency of about 400 cps; only for the largest plug openings the frequency decreased in some cases to about 200 cps. In most records the existence of a small amplitude, low frequency oscillation was discernible; however, only in one case ($M_\infty = 1.64$, S = 0.5, Figure 21(a)) was the amplitude of the low frequency oscillations appreciable. A schlieren photograph corresponding to this case is shown in Figure 23(e), the Sierra cell being in the lower duct.

The amplitude of the high frequency oscillations was small, except for the smallest mass flow and for the case of no boundary layer bleed flow.

Although the oscillograph* records show in general high frequency, small amplitude pressure oscillations, they are not considered to imply the existence of intake flow conditions usually referred to as "buzz". The schlieren flow observations, described below, corroborate the above view, at least for full boundary layer bleed flow. Furthermore, the oscillograph trace corresponding to no-flow conditions, Figures 21 and 22, already contained frequencies of about 200 cps which were presumably present in the actual test records. It was found that this initial oscillation in the oscillograph record could not be isolated. Shock mounting the oscillograph to remove the effects of pump motor and tunnel vibration produced no change in the zero oscillation which was apparently electrical in origin. The uniformity in the frequencies obtained could not be attributed to frequency overloading. the pressure cells possessing true response characteristics to well over 400 cps.

Because of the lower duct static pressures at the higher mass flows, the initial prestressing of the cell diaphragm to avoid static loading during a test, often exceeded the rated 2.5 psi limit of the cell, see Table 1. However, these initial differentials were never maintained for any appreciable length of time and under these conditions the cells were capable of withstanding over 200% overloads.

7.5 Schlieren Photographs

A typical series of schlieren photographs taken at a Mach number of 1.64 are presented in Figures 23 to 25 inclusive. These were obtained at zero incidence and with the original ramps, the model being rolled 90° as described in section 5.

Figures 23(a) and 23(b) are repeat runs which show the flow configurations on the body with natural external transition, no boundary layer bleed flow and minimum mass flow through the intakes (S = 0.5). These runs demonstrated the unsteady nature of the separation which occurred just downstream of the fore-

* The oscillograph frequency response was flat to 750 c.p.s.

body bulge. In Figure 23(a) this separation took place on the starboard (lower) side of the forebody while on the port side separation took place slightly upstream of the ramp lip. This resulted in a highly asymmetrical shock pattern at the entry to the intakes, there being in fact no shock system on the starboard ramp. When forebody separation alternated to the port side, as shown in Figure 23(b), separation upstream of the starboard ramp did not occur and the normal shock on the ramp moved closer to the intake entry. This alternative location of separation was not regular and indicated some type of flow instability. The phonomenon was unpredictable in that it could not be ascertained whether the side on which separation first occurred was fixed by tunnel starting conditions or whether the changeover occurred during a tunnel run.

Figures 23(c) and 23(d) show the effect of increasing mass flow on forebody separation and on entry shock configuration. At medium mass flows (S = 0.7), Figure 22(c), forebody separation occurred further downstream while the normal shock on the ramp moved closer to the entry. At the highest mass flow investigated (S = 0.9), Figure 23(d), separation occurred only on the starboard side, slightly upstream of the ramp lip and the normal entry shock occurred closer to the entry face.

With full boundary layer bleed flow, Figures 23(e) and (g) inclusive, no forebody separation obtained; again the progressive downstream movement of the normal shock on the ramps with increasing mass flow was clearly seen, the shock being unswallowed at the highest mass flow (S = 0.9).

Induced transition, achieved as described in section 7.1, produced the effects shown in Figure 24. In Figures 24(a) to (c) inclusive, the mass flow in the intakes was increased for no boundary bleed flow. Hence these figures correspond to Figures 23(a), (c) and (d) where transition was natural. Inducing transition can be seen to delay separation to a point further downstream but prevented it only at the highest mass flow, in one intake only.

When the flow in the boundary layer bleed ducts was nominally one half (exit area equal to one half the fully open area) the external flow configurations are given in Figures 24(d) to (f) for increasing mass flow in the intakes. Figures 24(g) to (i) give the corresponding configurations with full boundary layer bleed flow (exit area equal to fully open value).

A notable fact concerning the Sierra records is the lack of correlation with the schlieren photographs of the flow at the duct entries. The photographs corresponding to the Sierra cell records of Figure 22 are shown in Figure 25 where the cell was in the lower duct. Here it is seen that separation had occurred

well ahead of the intake ramps yet the dynamic pressure records have the same regular appearance as those taken for the flow configurations represented in Figures 23(f) and (g) where no separation had taken place. Also Figure 23(e) shows no occurrence of separation on the forebody yet the corresponding Sierra cell record (Figure 21(a)) as mentioned in section 7.4 exhibited an irregular oscillation in amplitude.

In addition to the investigation of flow stability by means of the Sierra cell, several schlieren photographs were taken for each configuration both by double exposure spark and by repeated single photographs. The latter were superimposed. But in either case no movement of the shock system on the intake ramps could be detected.

8. Conclusions

(i) The velocity distribution in the intake ducts at the subsonic diffuser exit was found to be highly non uniform. This was attributed to the internal duct configuration, including poor matching of the internal flow surfaces in the intake model and made the evaluation of results laborious and inaccurate.

(ii) The pressure recovery as determined experimentally was found to be appreciably smaller than that obtained with basically similar models by the N.A.C.A.; see Figure 26.

(iii) The total external intake drag (i.e. spillage drag plus fuselage forebody drag) was measured and its variation with mass flow determined.

(iv) Flow stability in the intake subsonic diffusor was investigated by means of a strain gauge pressure transducer. Although the results could not be considered conclusive, it appeared that the "buzz" did not occur under full boundary layer bleed flow conditions.

(v) Double exposure and repeated spark schlieren photographs of the intake flow indicated stable conditions with full boundary layer bleed flow.

(vi) Spark schlieren photographs of the intake were taken and have shown that no separation occurred ahead of the ramps with full boundary layer bleed flow. Severe separations were observed with boundary layer bleed partially or completely closed.

(vii) It was found that the non-uniformity of the velocity distribution at the subsonic diffuser exit was little affected by closing-off of the boundary layer bleed, by inducing boundary layer transition on the fuselage nose and on the ramp lips, by positive fuselage incidence and by eliminating leaks which were originally present in the model between the main and the boundary layer bleed ducts.

(viii) It was found that closing-off of the boundary layer bleed flow and/or inducing transition on the fuselage nose and on the ramp lips decreased appreciably (by about 10 percent) the pressure recovery; positive incidence and sealing of the model had no effect on pressure recovery.

References

1. Letter from W. Czerwinski, Avro Aircraft Ltd., Aircfaft Engineering Division, Ref. No. 8362/31/J, January 12, 1955.

2. Joseph Davids, George A. Wise — Investigation at Mach numbers 1.5 and 1.7 of Twin-Duct Side Intake System with Two-Dimensional 6° Compression Ramps Mounted on a Supersonic Airplane. NACA RM E53H19 October 1953.

3. Paul C. Simon — Performance Characteristics at Mach numbers to 2.0 of Various Types of Side Inlets Mounted on Fuselage of Proposed Supersonic Airplane. IV - Rectangular-Cowl Inlets with Two-Dimensional Compression Ramps. NACA RM E52H29 October 1952.

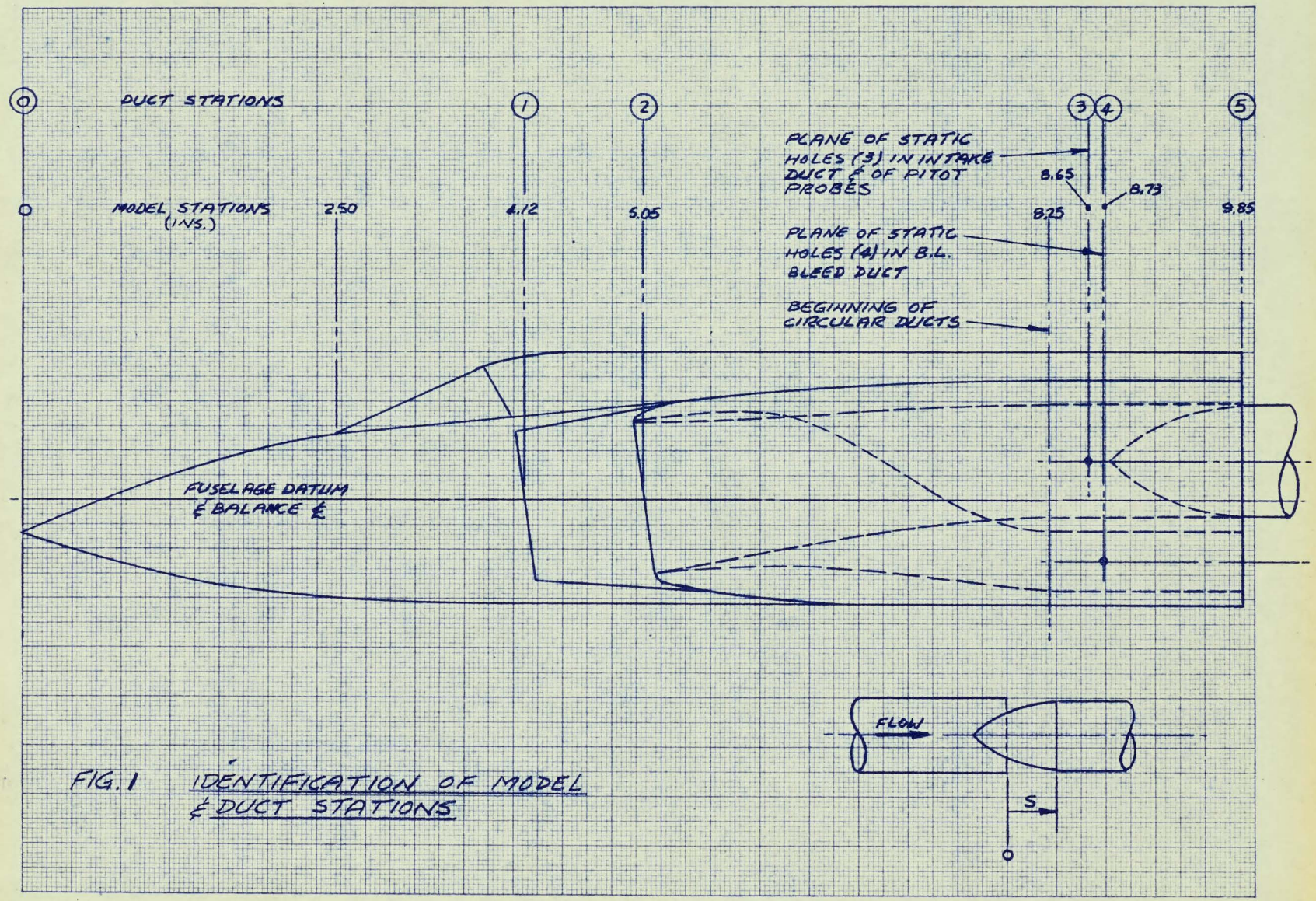

FIG. 1 IDENTIFICATION OF MODEL & DUCT STATIONS

TABLE 1

SIERRA CELL MEASUREMENTS

CHOKING PLUG POSITION S	BOUNDARY LAYER BLEED FLOW	α	M_∞	PRELOAD STATIC SHIFT (PSI)	DYNAMIC AMPLITUDE (PSI)	FREQUENCY (CPS)
0.5	FULL	0°	1.44	1.6	0.2	400
0.6				2.0	0.2	400
0.7				2.5	0.2	400
0.8				3.4	0.2	400
0.9				5.8	0.2	400
0.5	FULL	0°	1.64	3.1	3.0	400
0.6				3.3	1.4	400
0.7				3.6	0.4	400
0.8				4.2	0.4	400
0.9				6.5	0.4	200
0.5	FULL	0°	1.83	4.2	1.2	400
0.6				4.4	0.8	400
0.7				4.5	0.5	350
0.8				4.9	0.4	300
0.9				6.8	0.4	200
0.5	ZERO	0°	1.83	4.9	8.0	370
0.6				5.0	6.0	380
0.7				5.6	4.0	400
0.8				6.4	2.0	400
0.9				7.9	1.0	400

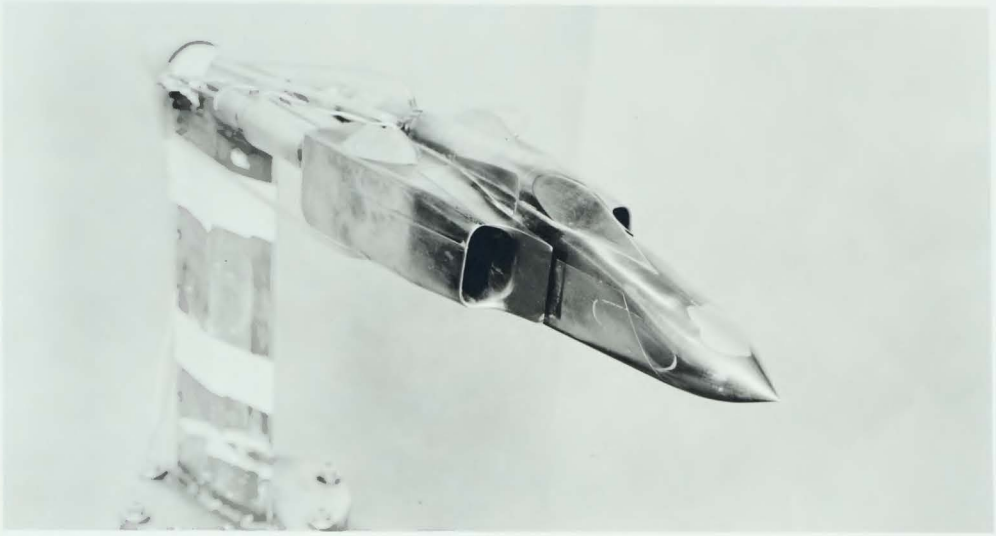

(a) GENERAL VIEW SHOWING INTAKES

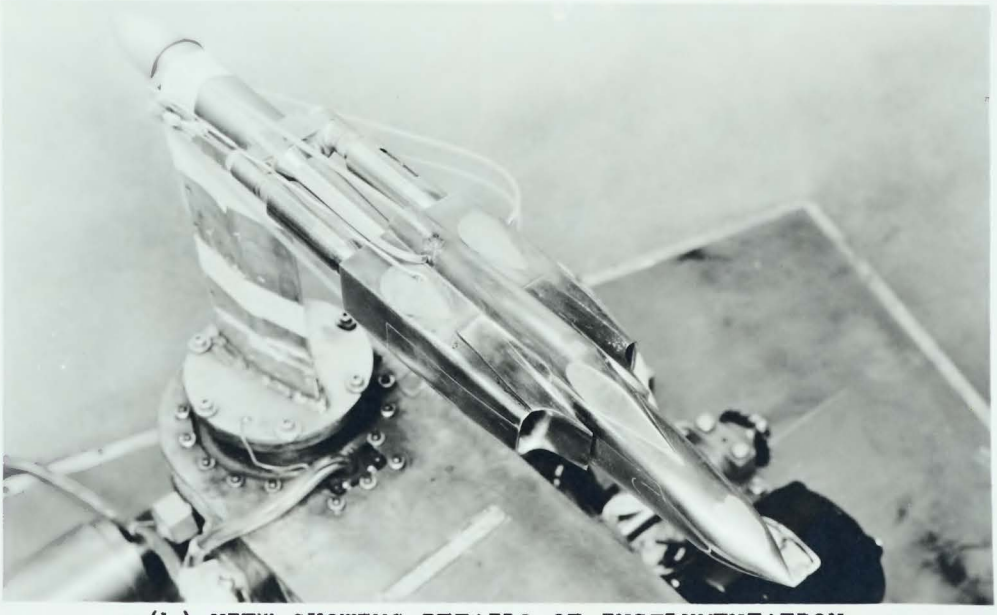

(b) VIEW SHOWING DETAILS OF INSTRUMENTATION

FIG. 2 MODEL MOUNTED ON BALANCE

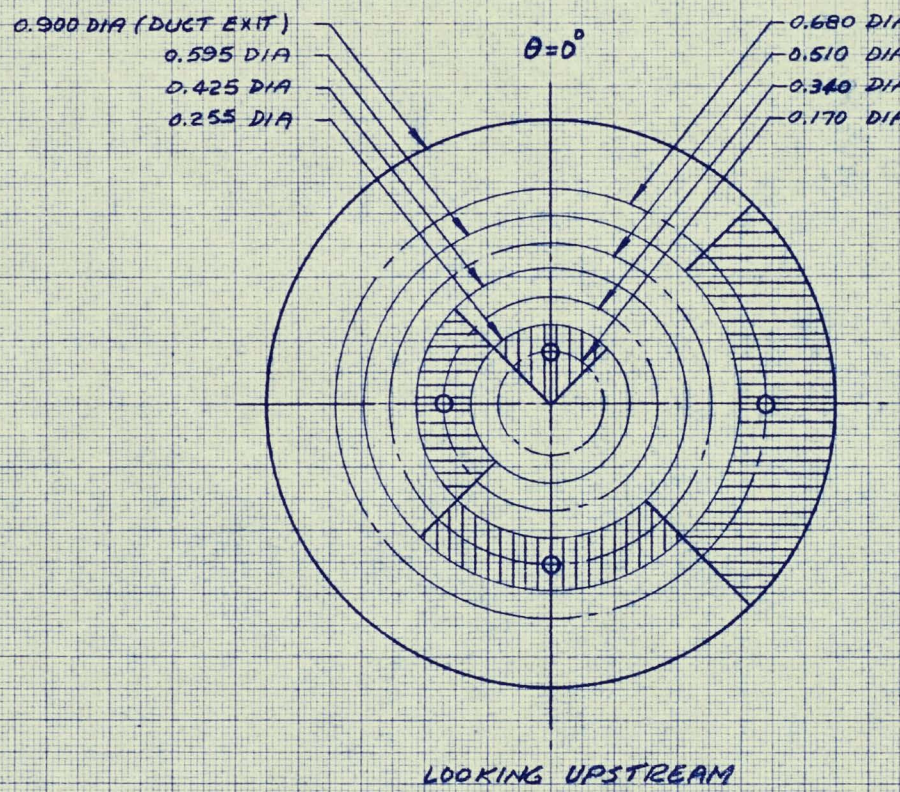

O PITOT PROBES

PROBE n	AREA OF DIVISION $A_{3,n}$
1	$A_{3,1} = 0.0128$ IN.^{2}
2	$A_{3,2} = 0.0227$
3	$A_{3,3} = 0.0342$
4	$A_{3,4} = 0.0895$

FIG. 4 PITOT PROBE LOCATION & ASSOCIATED AREA DIVISIONS

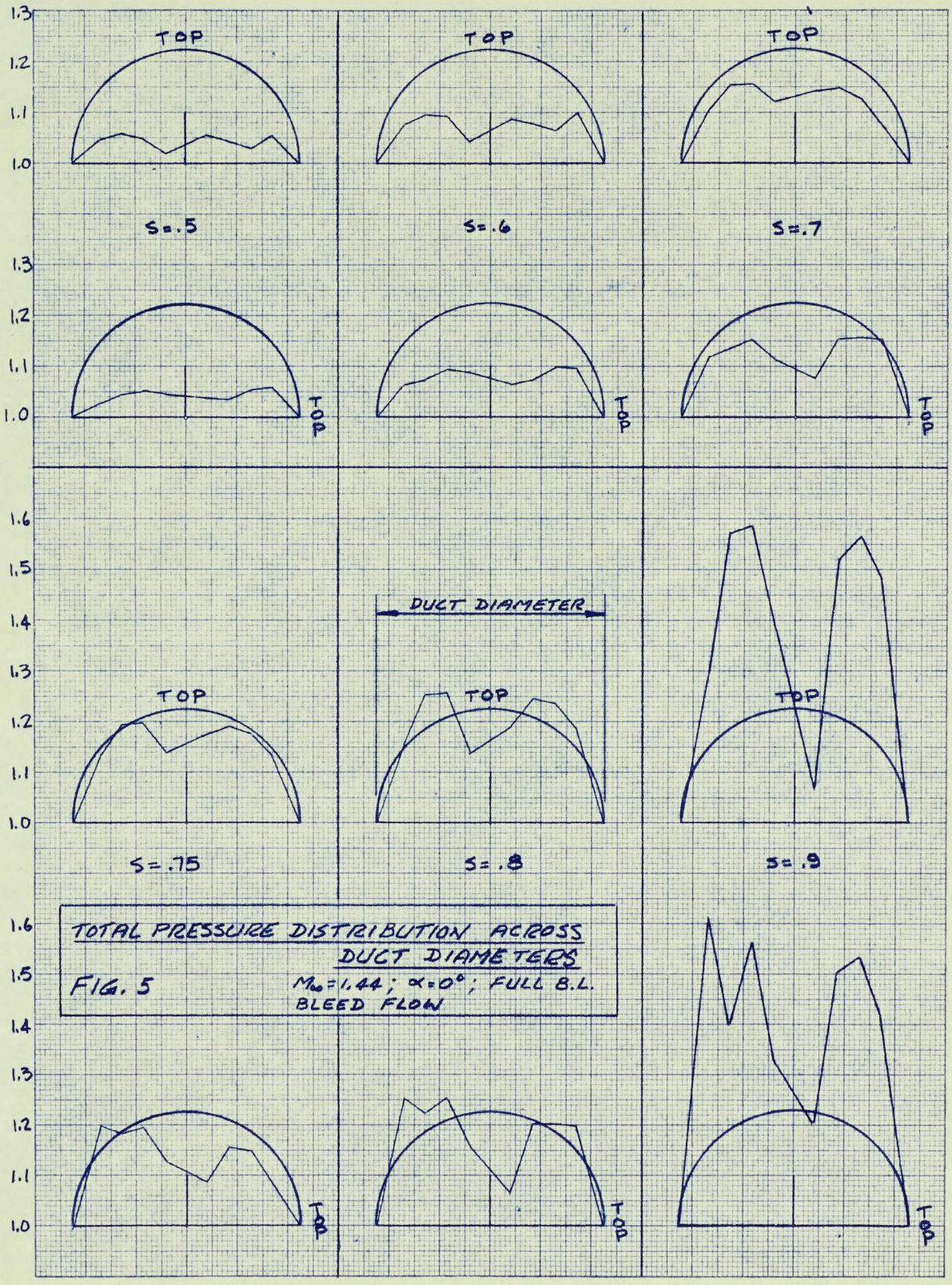

TOTAL PRESSURE DISTRIBUTION ACROSS DUCT DIAMETERS

FIG. 5

$M_\infty = 1.44$; $\alpha = 0°$; FULL B.L. BLEED FLOW

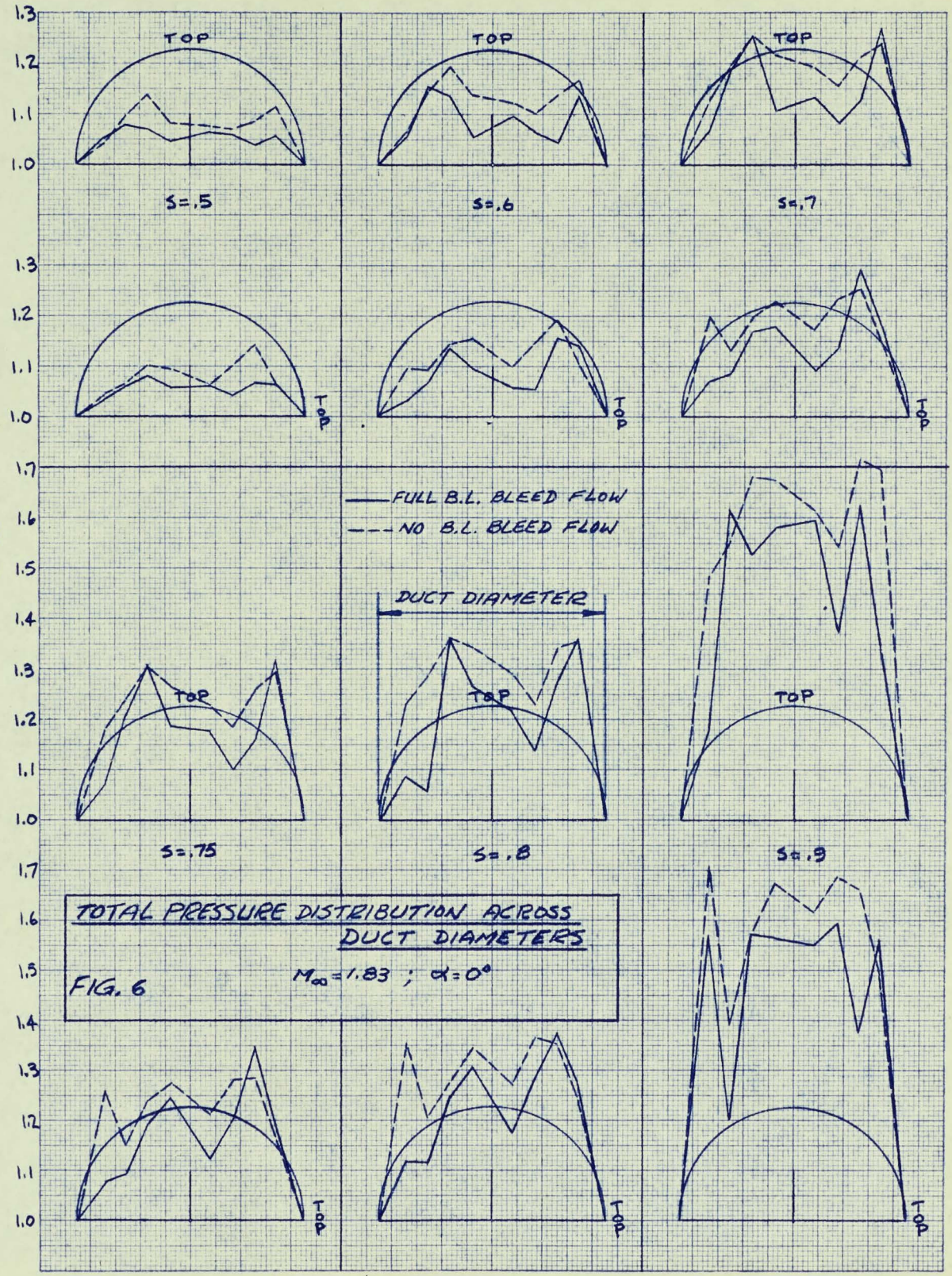

TOTAL PRESSURE DISTRIBUTION ACROSS DUCT DIAMETERS

FIG. 6 $M_\infty = 1.83$; $\alpha = 0°$

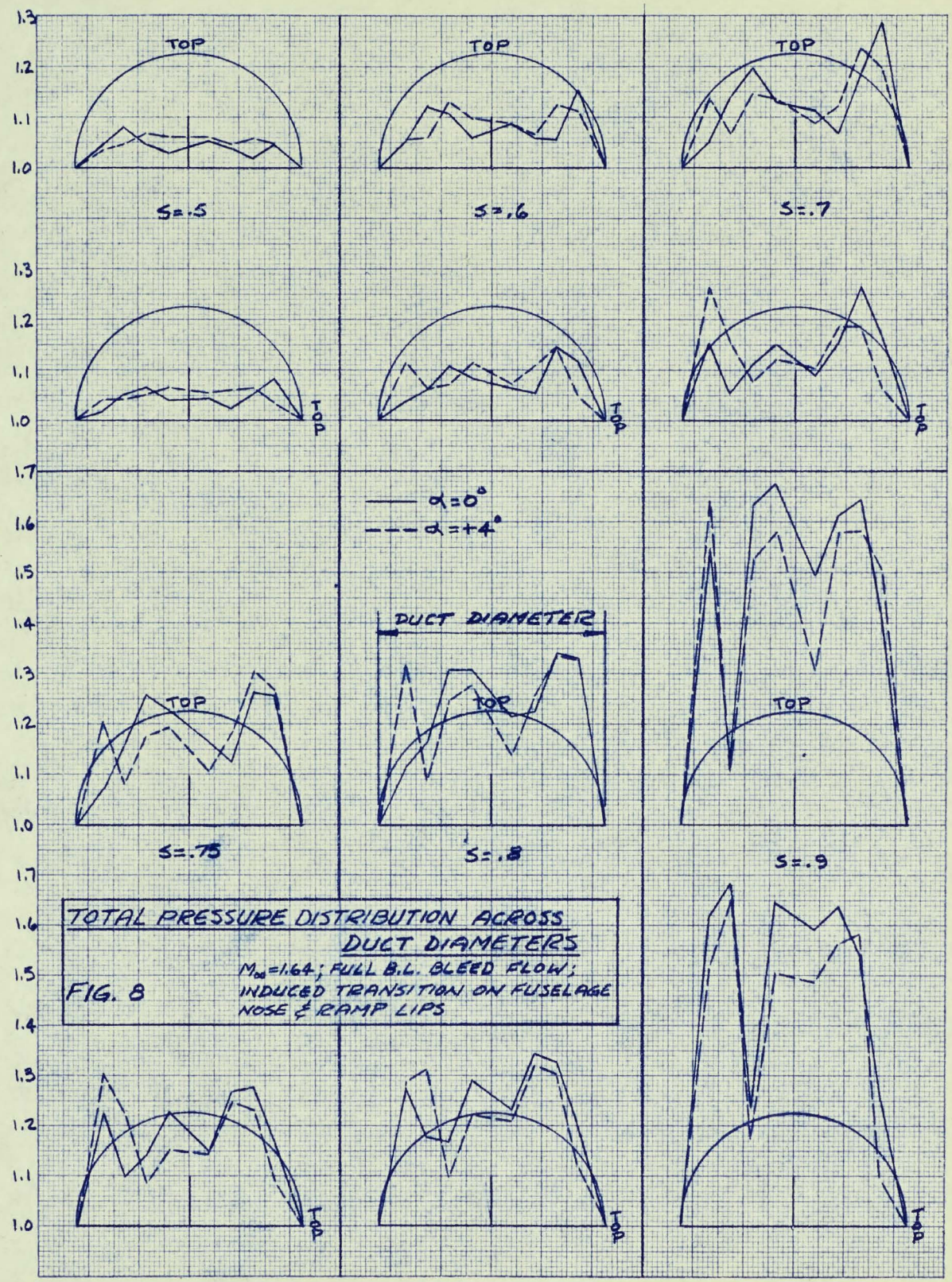

TOTAL PRESSURE DISTRIBUTION ACROSS DUCT DIAMETERS

FIG. 8

M_∞=1.64; FULL B.L. BLEED FLOW; INDUCED TRANSITION ON FUSELAGE NOSE & RAMP LIPS

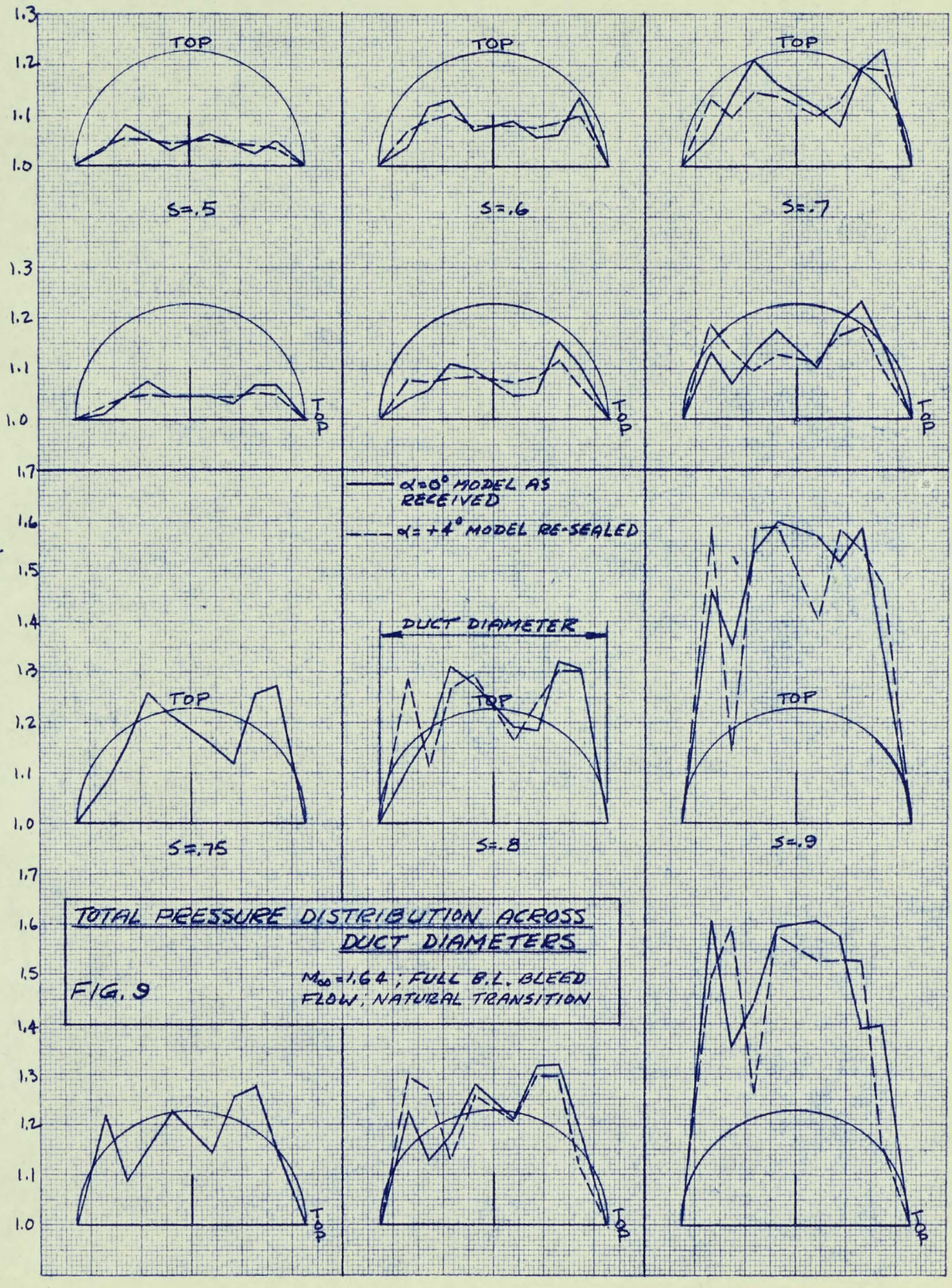

TOTAL PRESSURE DISTRIBUTION ACROSS DUCT DIAMETERS

FIG. 9

M_∞=1.64; FULL B.L. BLEED FLOW; NATURAL TRANSITION

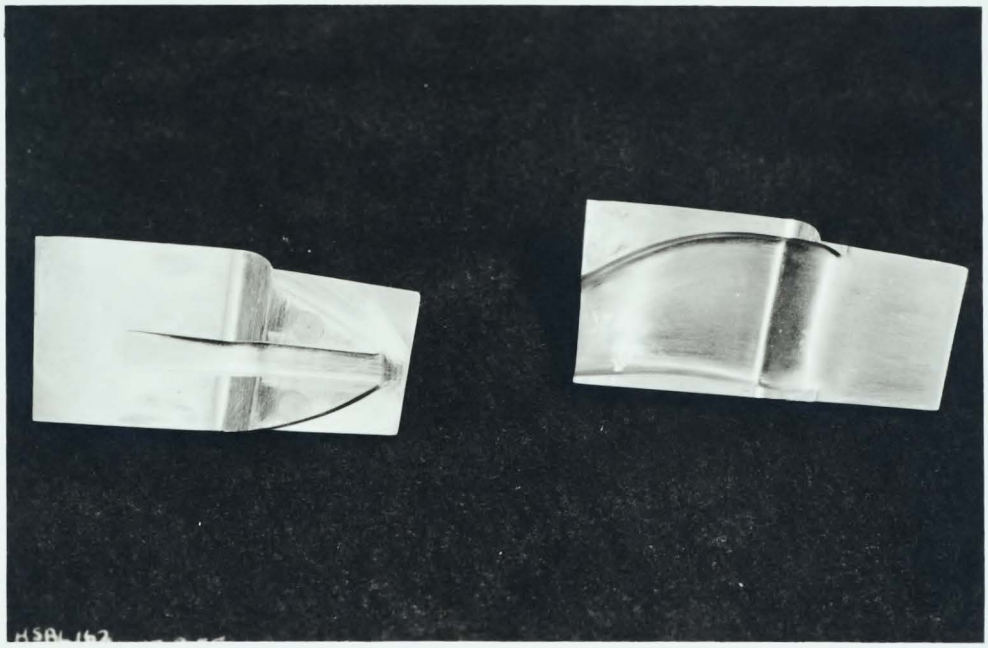

FIG. 10 DETAILS OF THE TWO TYPES OF BOUNDARY LAYER BLEED DUCT ENTRIES. MODIFIED ENTRY ON THE LEFT.

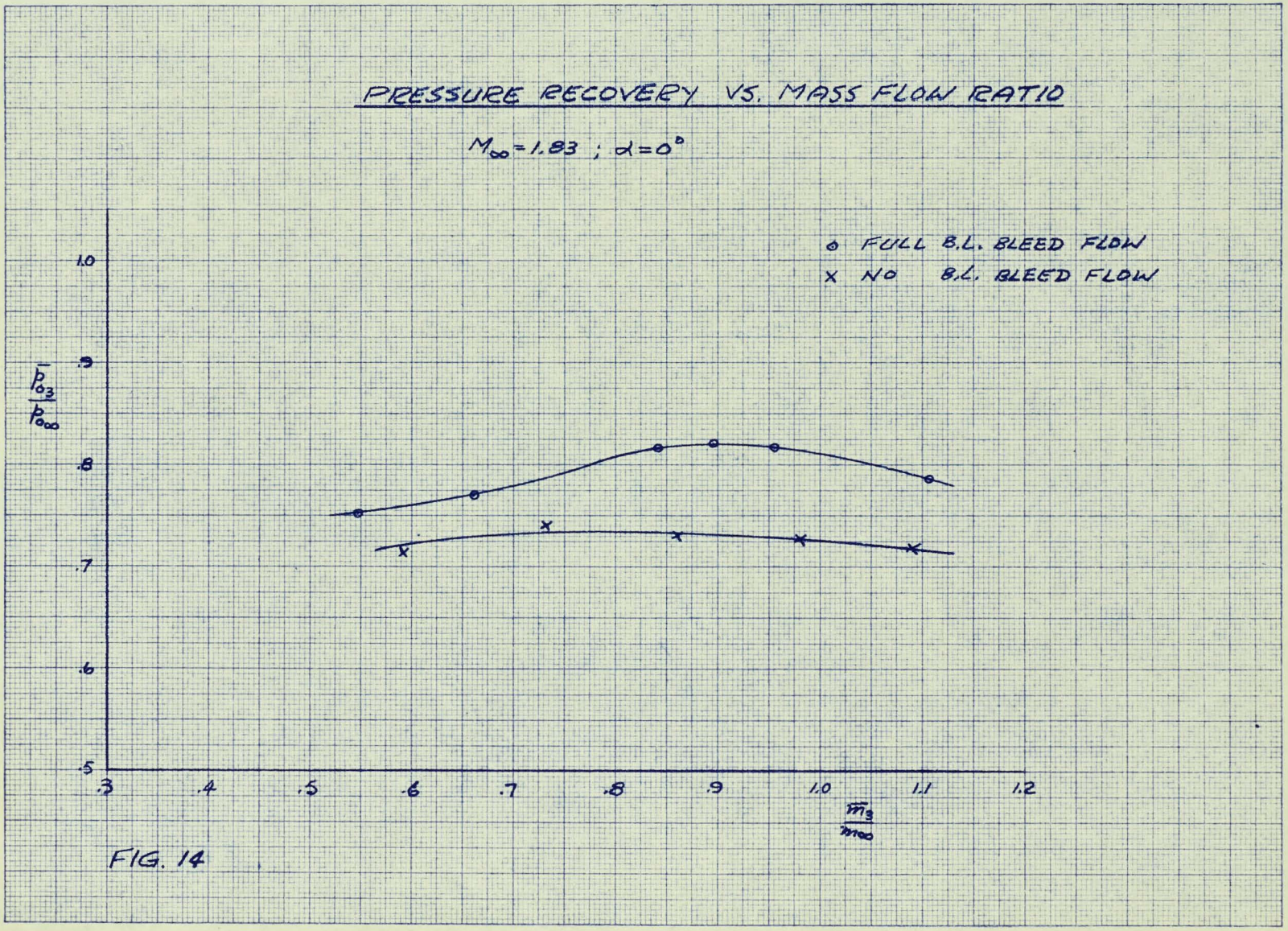

FIG. 14

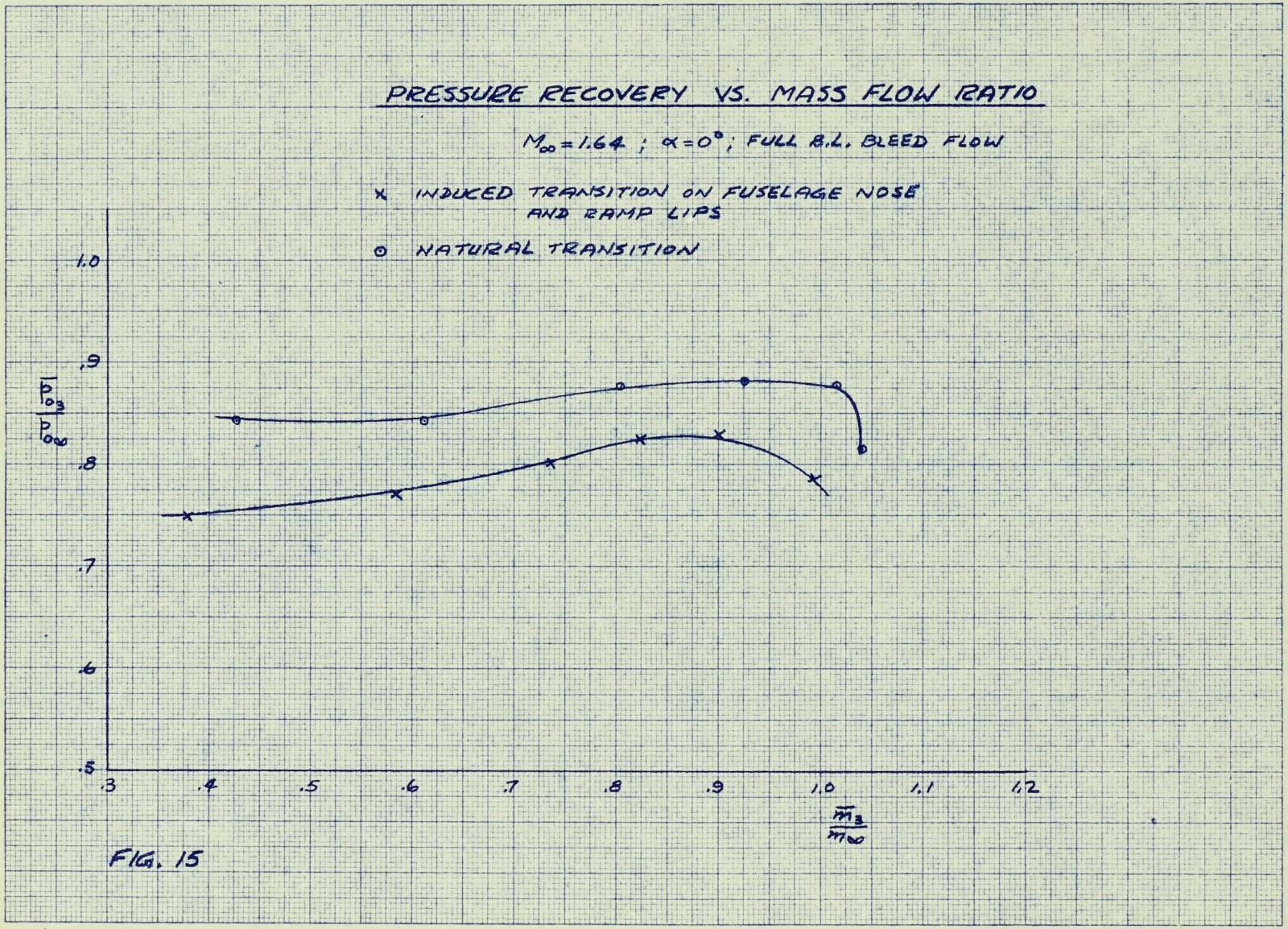

FIG. 15

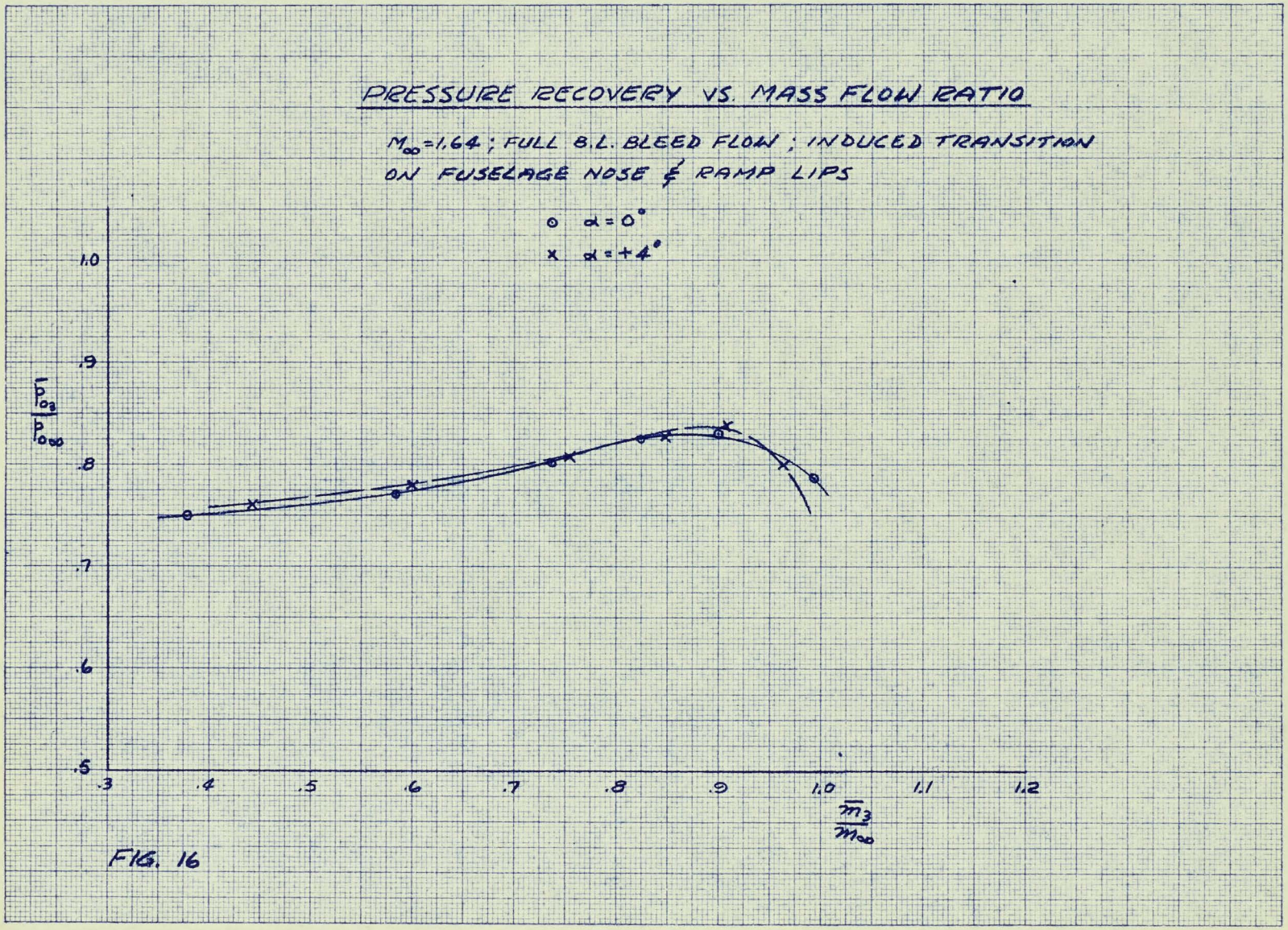

FIG. 16

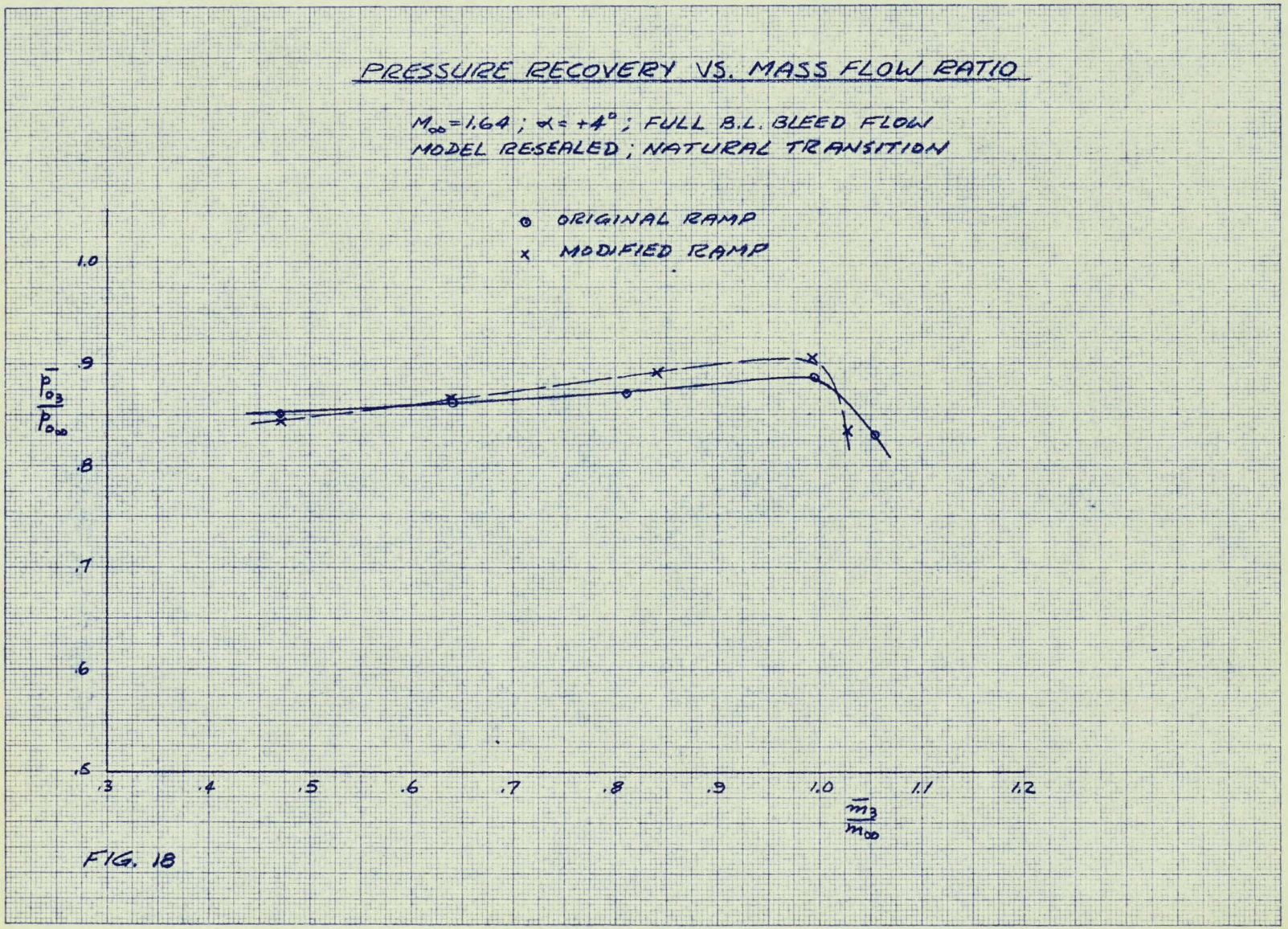

FIG. 18

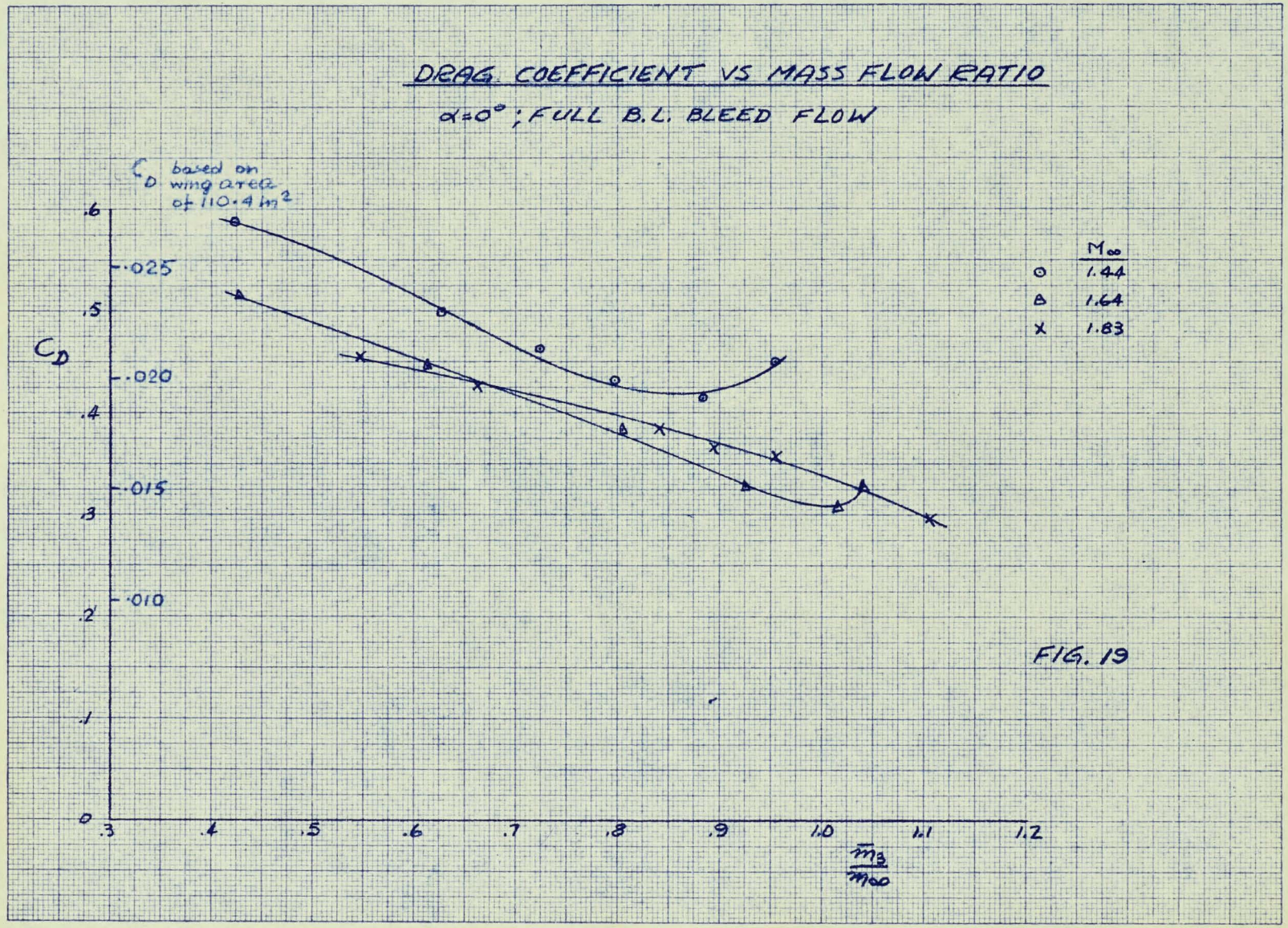

FIG. 19

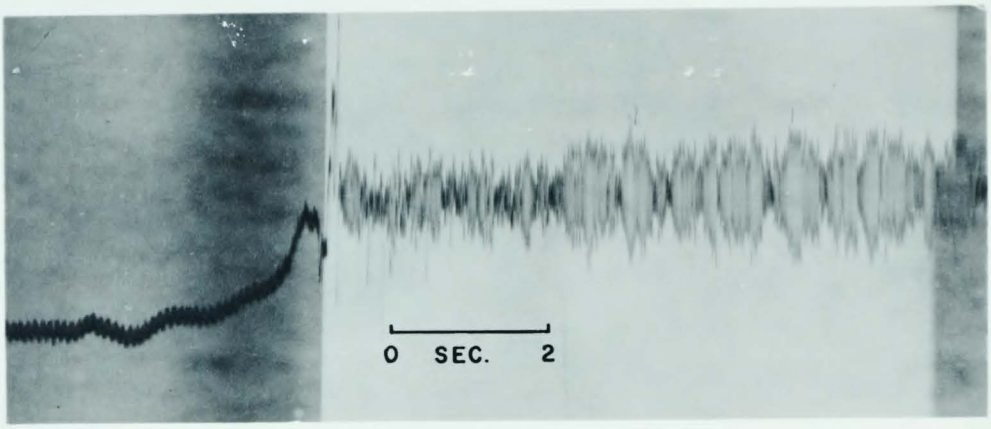

(a) S=.5, DYNAMIC AMPLITUDE= 3.0 PSI, FREQ.=400 CPS.

(b) S=.6, DYNAMIC AMPLITUDE = 1.4 PSI, FREQ.= 400 CPS.

FIG.21 OSCILLOGRAPH RECORDS M_∞ = 1.64
FULL BOUNDARY LAYER BLEED FLOW

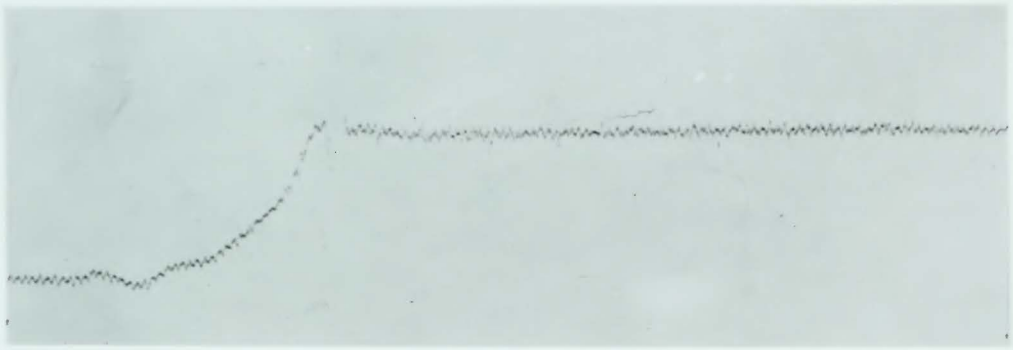

(c) S=.7, DYNAMIC AMPLITUDE = 0.4 PSI, FREQ.= 400 CPS.

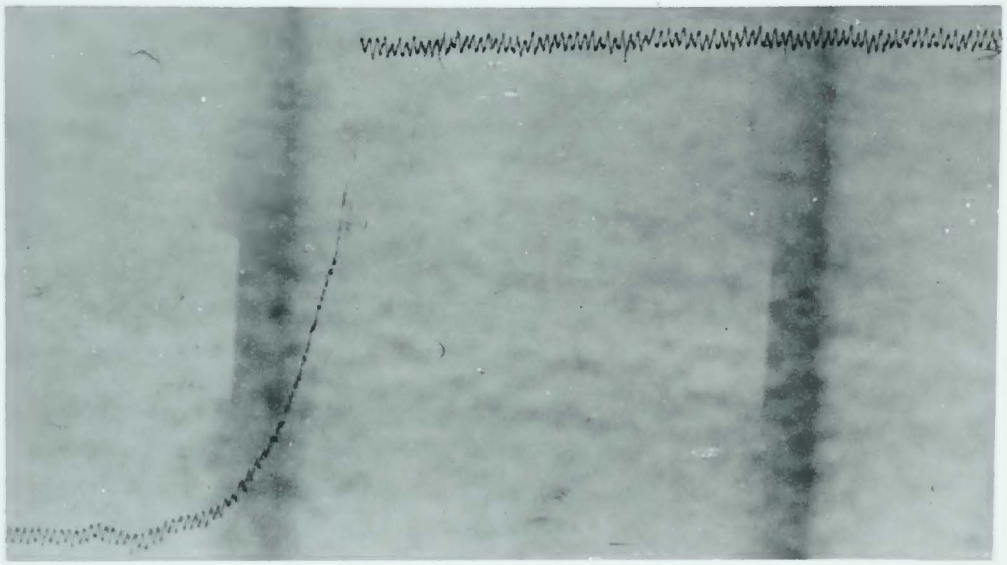

(d) S=.9, DYNAMIC AMPLITUDE = 0.4 PSI, FREQ.= 200 CPS.

FIG.21 (CONCLUDED)

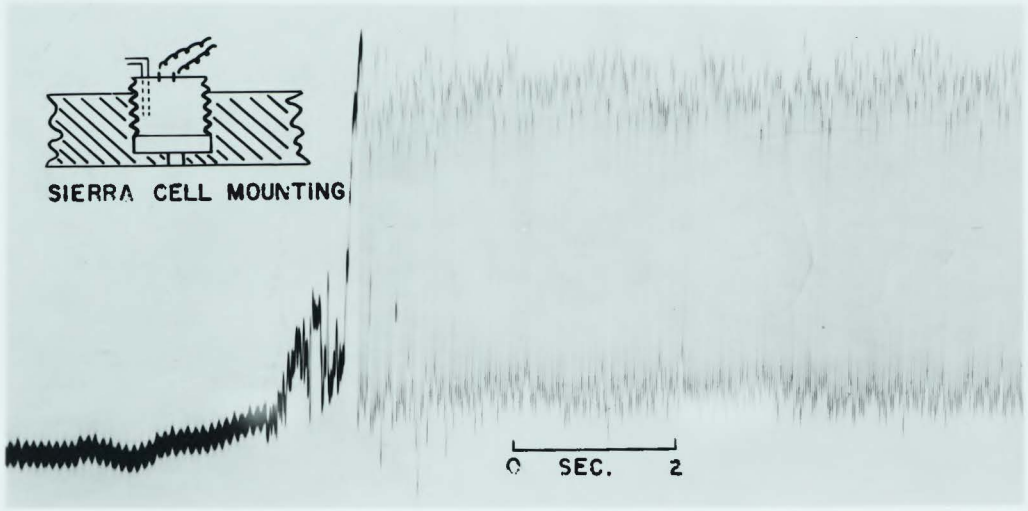

(a) S=.5, DYNAMIC AMPLITUDE = 8.0 PSI, FREQ.= 370 CPS

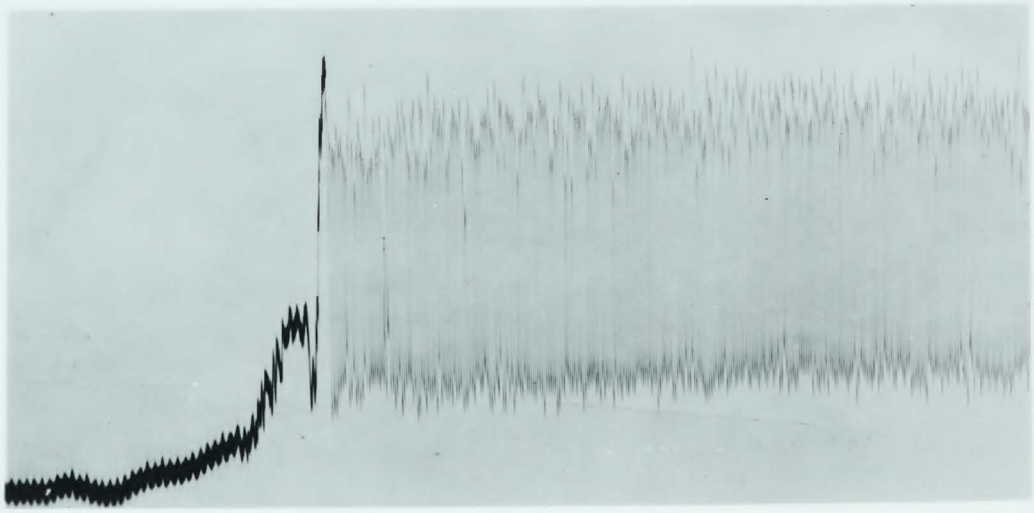

(b) S=.6, DYNAMIC AMPLITUDE = 6.0 PSI, FREQ.= 380 CPS

FIG.22 OSCILLOGRAPH RECORDS $M_\infty = 1.83$
NO BOUNDARY LAYER BLEED FLOW

(c) S=.7, DYNAMIC AMPLITUDE = 4.0 PSI, FREQ.= 400 CPS

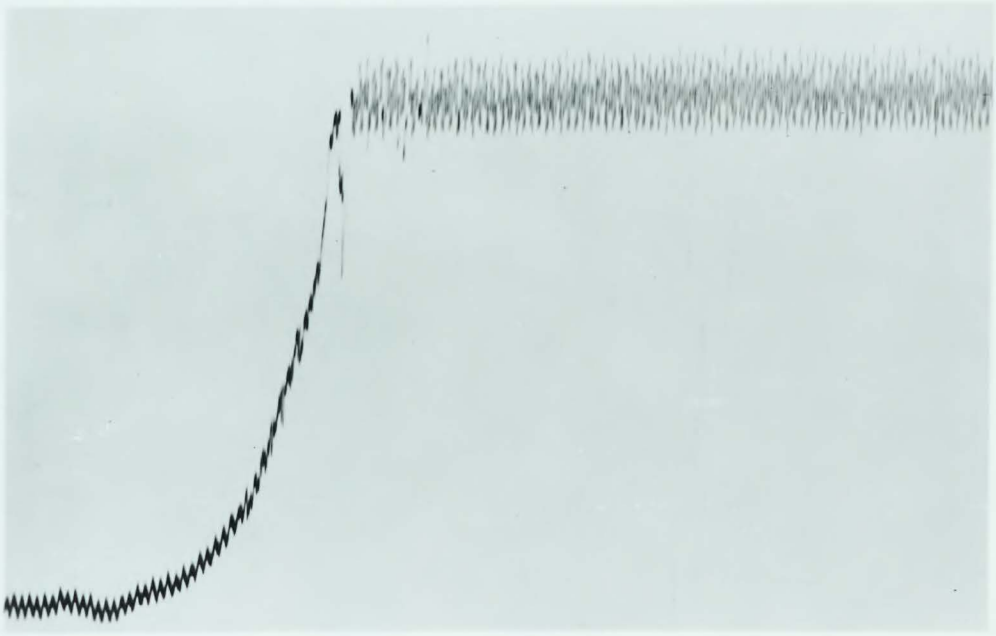

(d) S=.9, DYNAMIC AMPLITUDE = 1.0 PSI, FREQ.= 400 CPS

FIG.22 (CONCLUDED)

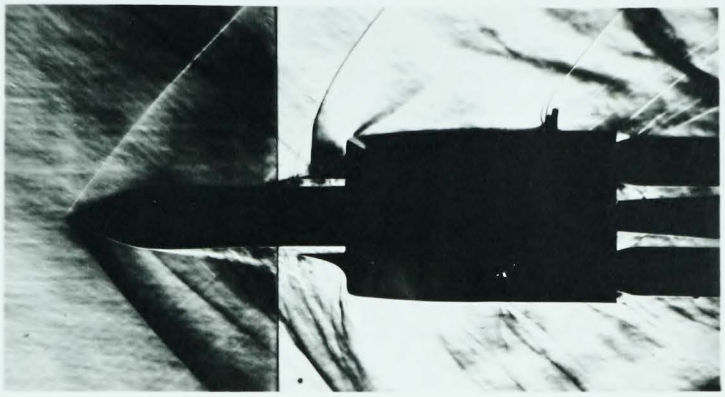

(a) S=.5, NO BOUNDARY LAYER BLEED FLOW

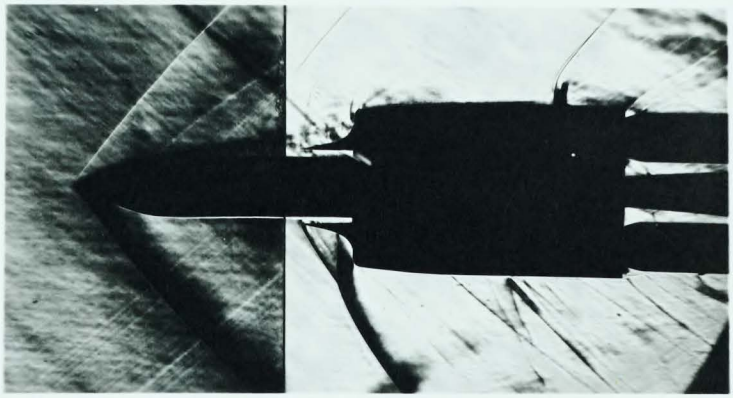

(b) REPEAT OF (a) SHOWING AN ALTERNATIVE POSITION OF SEPARATION

FIG.23 SCHLIEREN PHOTOGRAPHS M_∞ = 1.64
NATURAL TRANSITION

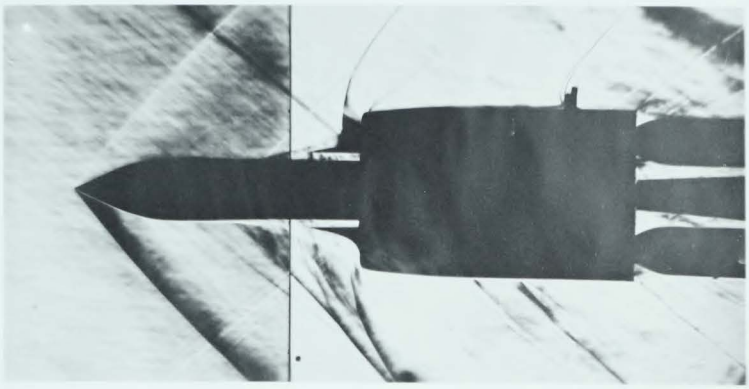

(c) S=.7, NO BOUNDARY LAYER BLEED FLOW

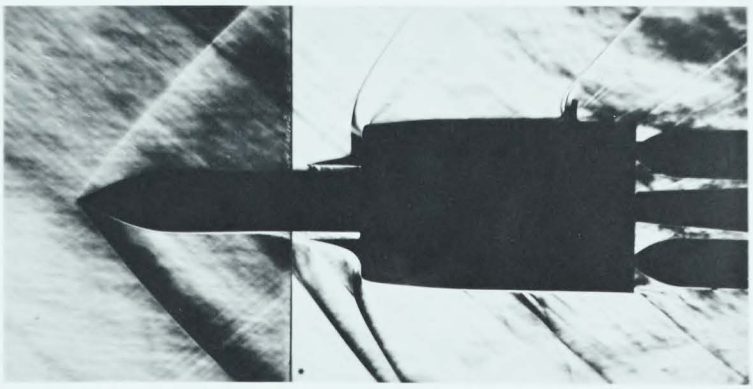

(d) S=.9, NO BOUNDARY LAYER BLEED FLOW

FIG.23 (CONTINUED)

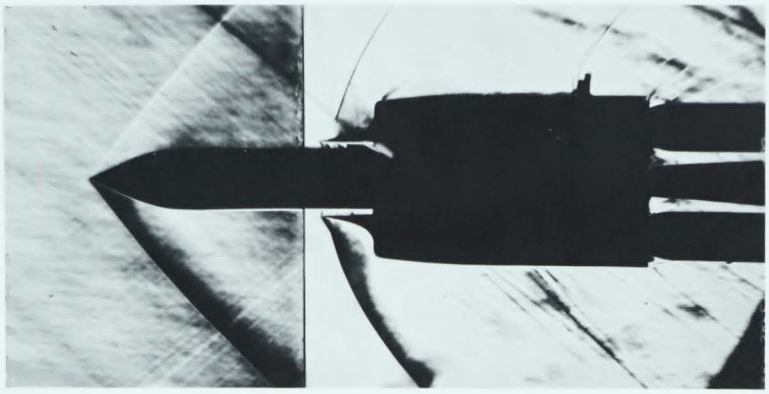

(e) S=.5, FULL BOUNDARY LAYER BLEED FLOW

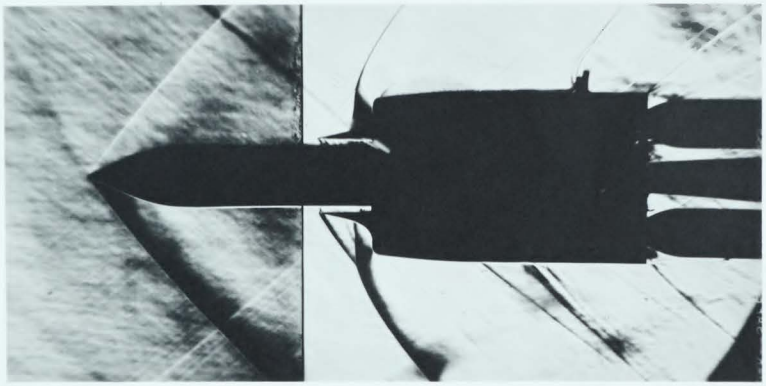

(f) S=.7, FULL BOUNDARY LAYER BLEED FLOW

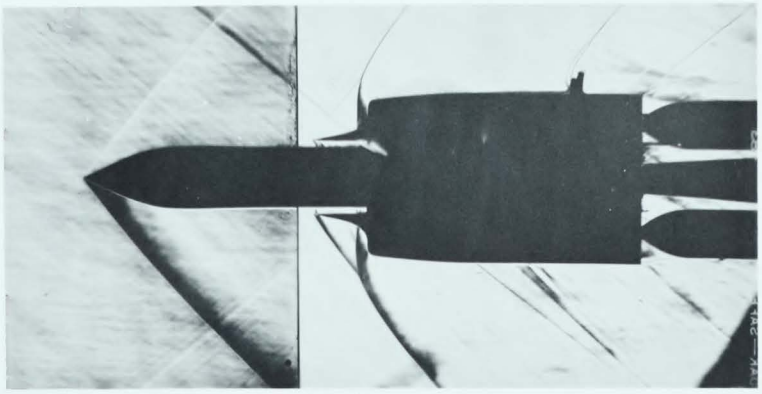

(g) S=.9, FULL BOUNDARY LAYER BLEED FLOW

FIG.23 (CONCLUDED)

(a) S=.5, NO BOUNDARY LAYER BLEED FLOW

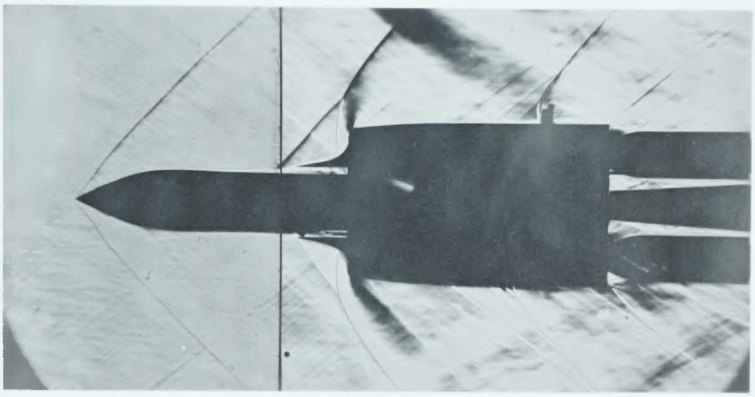

(b) S=.7, NO BOUNDARY LAYER BLEED FLOW

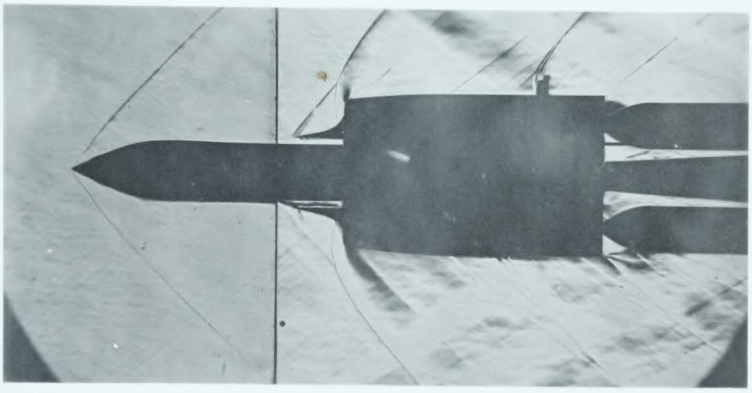

(c) S=.9, NO BOUNDARY LAYER BLEED FLOW

FIG.24 SCHLIEREN PHOTOGRAPHS M_∞ = 1.64
INDUCED TRANSITION

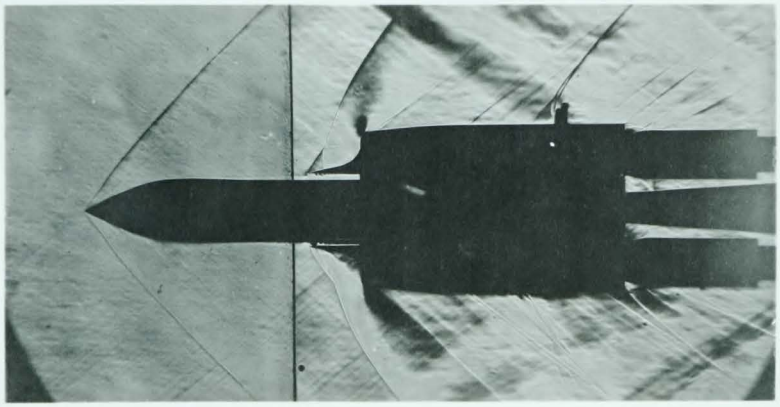

(d) S=.5, HALF BOUNDARY LAYER BLEED FLOW

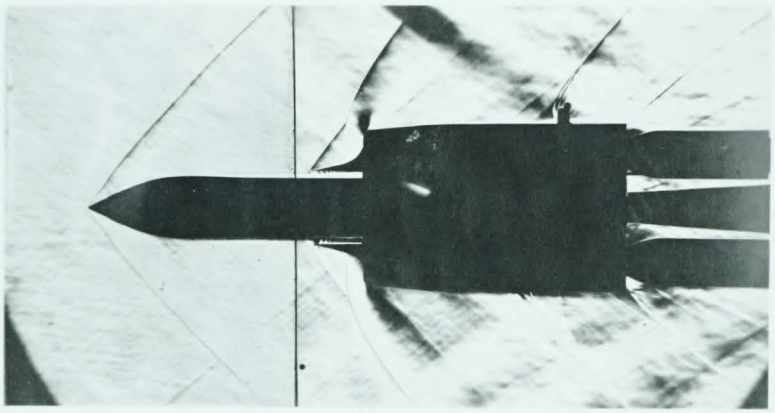

(e) S=.7, HALF BOUNDARY LAYER BLEED FLOW

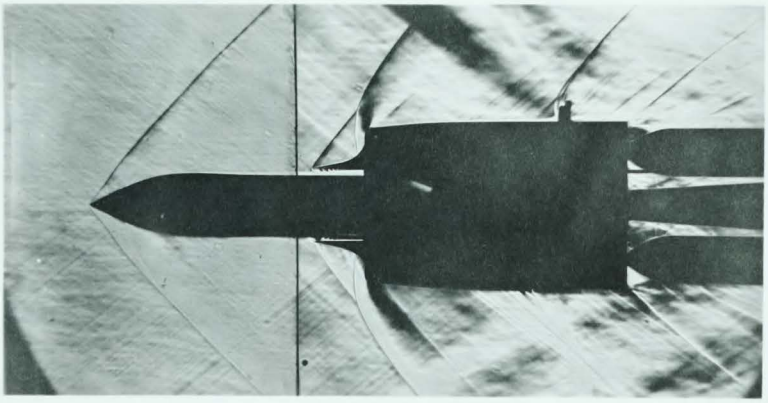

(f) S=.9, HALF BOUNDARY LAYER BLEED FLOW

FIG.24 (CONTINUED)

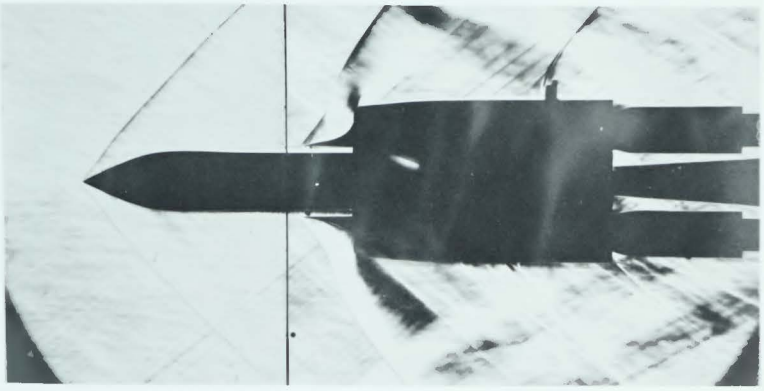

(g) S=.5, FULL BOUNDARY LAYER BLEED FLOW

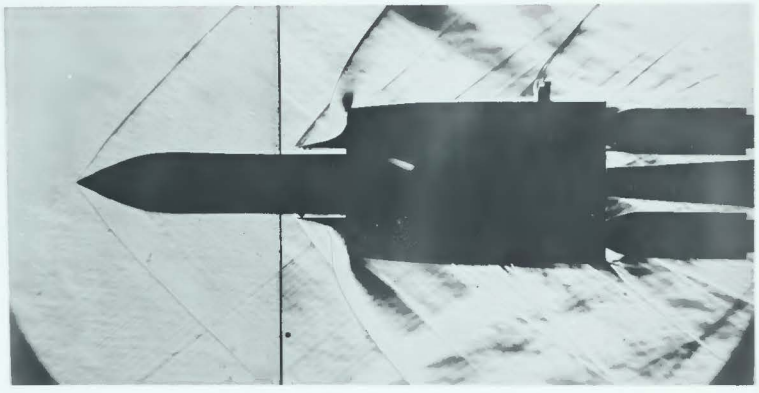

(h) S=.7, FULL BOUNDARY LAYER BLEED FLOW

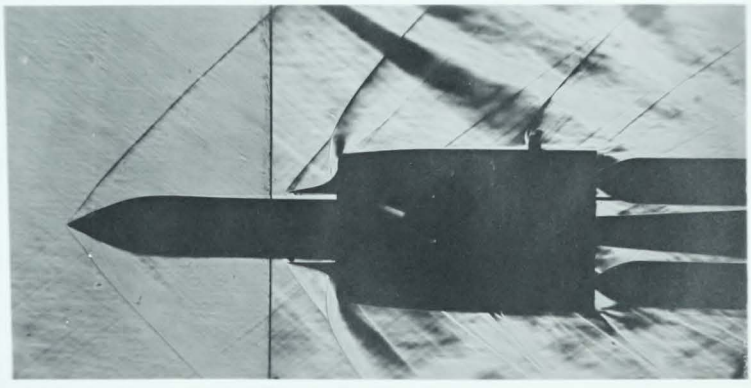

(i) S=.9, FULL BOUNDARY LAYER BLEED FLOW

FIG. 24 (CONCLUDED)